2021

Dynamic Characteristics of DC-DC Converters with Coupled and Nonlinear Magnetics

Chaitanya Inamdar
Michigan Technological University, csinamda@mtu.edu

DYNAMIC CHARACTERISTICS OF DC-DC CONVERTERS WITH COUPLED AND NONLINEAR MAGNETICS

By

Chaitanya S. Inamdar

A THESIS

Submitted in partial fulfillment of the requirements for the degree of

MASTER OF SCIENCE

In Electrical and Computer Engineering

MICHIGAN TECHNOLOGICAL UNIVERSITY

2021

This thesis has been approved in partial fulfillment of the requirements for the Degree of MASTER OF SCIENCE in Electrical and Computer Engineering.

Department of Electrical and Computer Engineering

Thesis Advisor:	*Dr. Wayne W. Weaver*
Committee Member:	*Dr. Yunting Liu*
Committee Member:	*Dr. Gordon G. Parker*
Department Chair:	*Dr. Glen E. Archer*

Dedication

To my family, especially my parents and sister,

who have supported me every step of the way, not just in this journey, but life.

Contents

List of Figures . . . . . **xi**

List of Tables . . . . . **xv**

Acknowledgments . . . . . **xvii**

Abstract . . . . . **xix**

1 Introduction **1**

1.1 Objective 1

1.2 Background 2

1.3 Thesis Overview 5

2 Mathematical models of converters **7**

2.1 Introduction 7

2.2 Boost converter with a linear inductor 8

2.3 Boost converter with a nonlinear saturating inductor 9

3 Boost converter with a coupled inductor and bleed off resistor . **11**

3.1 Proposed solution 11

3.2 Mathematical modeling 13

4 Applications and demonstration 23

4.1 Introduction 23

4.2 Minimum time response for a step increase in resistive load 24

4.2.1 Transition process for a boost converter with a nonlinear saturating inductor 24

4.2.2 Transition process for a CIBR boost converter 27

4.2.3 Comparison of the transition processes 35

4.3 Minimum time response for a step decrease in resistive load 36

4.3.1 Transition process for a boost converter with a nonlinear saturating inductor 37

4.3.2 Transition process for a CIBR boost converter 44

4.3.3 Comparison of the transition processes 53

4.4 Stability of pulsed power loads 54

4.4.1 Stability map for a boost converter with a linear inductor . . 55

4.4.2 Stability map for a CIBR boost converter 60

4.4.3 Comparison of the stability maps 67

5 Conclusion and future work 73

5.1 Conclusion 73

5.2 Future work 74

References **77**

List of Figures

2.1 Boost converter with a linear inductor 8

2.2 Boost converter with a nonlinear saturating inductor 9

3.1 Boost converter with a coupled inductor and a bleed off resistor . . 12

3.2 Coupled inductor 13

4.1 Inductor current in the boost converter with a nonlinear saturating inductor for a step increase in load 27

4.2 Capacitor voltage in the boost converter with a nonlinear saturating inductor for a step increase in load 28

4.3 Current through the first coil of the CIBR boost converter for a step increase in load 33

4.4 Current through the second coil of the CIBR boost converter for a step increase in load 34

4.5 Total flux in the inductor core of the CIBR boost converter for a step increase in load 34

4.6 Capacitor voltage of the CIBR boost converter for a step increase in load 35

4.7 Inductor current in the boost converter with a nonlinear saturating inductor for a step decrease in load (CCM) 42

4.8 Capacitor voltage in the boost converter with a nonlinear saturating inductor for a step decrease in load (CCM) 43

4.9 Inductor current in the boost converter with a nonlinear saturating inductor for a step decrease in load (DCM) 45

4.10 Capacitor voltage in the boost converter with a nonlinear saturating inductor for a step decrease in load (DCM) 45

4.11 Coil 1 current in the CIBR boost converter for a step decrease in load (CCM-parameters) 50

4.12 Capacitor voltage in the CIBR boost converter for a step decrease in load (CCM-parameters) 50

4.13 Coil 1 current in the CIBR boost converter for a step decrease in load (DCM-parameters) 52

4.14 Capacitor voltage in the CIBR boost converter for a step decrease in load (DCM-parameters) 53

4.15 Boost converter with a linear inductor with a pulsed power load . . 55

4.16 Pulsed power loads 56

4.17 Inductor current for boost converter with a linear inductor with a pulsed power load when system is stable ($P = 6kW, Tp = 0.2s, Dp = 0.2$) 58

4.18 Output voltage for boost converter with a linear inductor with a pulsed power load when system is stable ($P = 6kW, Tp = 0.2s, Dp = 0.2$) . 59

4.19 Inductor current for boost converter with a linear inductor with a pulsed power load when system is unstable ($P = 6kW, Tp = 0.2s, Dp = 0.6$) 59

4.20 Output voltage for boost converter with a linear inductor with a pulsed power load when system is unstable ($P = 6kW, Tp = 0.2s, Dp = 0.6$) 60

4.21 Stability map for boost converter with a linear inductor with a pulsed power load 61

4.22 CIBR boost converter with a pulsed power load 61

4.23 Inductor current for CIBR boost converter with a pulsed power load when system is stable ($P = 6kW, Tp = 0.2s, Dp = 0.6$) 64

4.24 Output voltage for CIBR boost converter with a pulsed power load when system is stable ($P = 6kW, Tp = 0.2s, Dp = 0.6$) 65

4.25 Inductor current for CIBR boost converter with a pulsed power load when system is unstable ($P = 6kW, Tp = 0.2s, Dp = 0.8$) 65

4.26 Output voltage for CIBR boost converter with a pulsed power load when system is unstable ($P = 6kW, Tp = 0.2s, Dp = 0.8$) 66

4.27 Stability map for CIBR boost converter with a pulsed power load . 67

4.28 Comparison of the stability maps 69

4.29 A slice of Figure 4.28 at 6kW 70

4.30 Zoomed in version of Figure 4.29 71

4.31 Stability margins for different nominal inductances for a CIBR boost converter with a pulsed power load ($P = 5kW$) 72

List of Tables

3.1 Inductor core parameters for T650-52 22

4.1 Parameters for simulating a step increase in load for a boost converter with a nonlinear saturating inductor 26

4.2 Performance metrics from the simulation of a step increase in load for a boost converter with a nonlinear saturating inductor 27

4.3 Parameters for simulating a step increase in load for a CIBR boost converter 32

4.4 Performance metrics from the simulation of a step increase in load for a CIBR boost converter 33

4.5 Comparison between boost converter with a nonlinear saturating inductor and CIBR boost converter 35

4.6 Parameters for simulating a step decrease in load for a boost converter with a nonlinear saturating inductor (CCM) 41

4.7 Performance metrics from the simulation of a step decrease in load for a boost converter with a nonlinear saturating inductor (CCM) . . . 42

4.8 Parameters for simulating a step decrease in load for a boost converter with a nonlinear saturating inductor (DCM) 43
4.9 Performance metrics from the simulation of a step decrease in load for a boost converter with a nonlinear saturating inductor (DCM) . . . 44
4.10 Parameters for simulating a step decrease in load for a CIBR boost converter (CCM-parameters) 48
4.11 Performance metrics from the simulation of a step decrease in load for a CIBR boost converter (CCM-parameters) 49
4.12 Parameters for simulating a step decrease in load for a CIBR boost converter (DCM-parameters) 51
4.13 Performance metrics from the simulation of a step decrease in load for a CIBR boost converter (DCM-parameters) 52
4.14 Comparison between boost converter with a nonlinear saturating inductor and CIBR boost converter (CCM-parameters) 54
4.15 Comparison between boost converter with a nonlinear saturating inductor and CIBR boost converter (DCM-parameters) 54
4.16 Parameters for simulating a boost converter with a linear inductor with a pulsed power load 57
4.17 Parameters for simulating a CIBR boost converter with a pulsed power load 63

Acknowledgments

I have had the support and encouragement from a multitude of people through this journey. I would like to start off by expressing my sincere gratitude to my advisor Dr. Wayne Weaver, and thank him for giving me this opportunity to learn. He has been incredibly patient and has provided continuous support. His guidance has helped me succeed in this endeavour. I would also like to thank my committee members Dr. Yunting Liu and Dr. Gordon Parker for dedicating their time and effort to be on my committee. I would also like to thank Trever Hassell for his support.

To all of my professors, family and friends, I will forever be grateful for your teachings and encouragement.

Abstract

As more and more industries move towards electrification of their processes and technologies, improving the dynamic characteristics of DC-DC converters stands to be beneficial across a wide range of applications. Modifications are made to a typical boost converter's topology in conjunction with a bang-bang control strategy (which has been shown to minimize the transition time), to improve the dynamic characteristics for step changes in load. Incorporating a coupled inductor instead of a normal inductor, and using the second coil of the coupled inductor to saturate the core helps to improve performance for step increases in load. Another modification made is the addition of a bleed-off resistor at the output capacitor, which burns off excess energy in the converter to improve performance when it comes to step decreases in load. This thesis also takes a brief look at the stability of pulsed power loads. Previously, the stability margins were mapped with a boost converter with a linear inductor model and constant duty cycle control. This thesis shows that those stability margins can be improved upon by using the new topology and bang-bang control.

Chapter 1

Introduction

1.1 Objective

The application of DC-DC converters is ubiquitous across many industries. These converters are used over a wide range of power levels [1][2]. They are utilized in appliances ranging from small battery powered devices [3], to large applications like electric vehicles [4][5]. Thus, any improvement in the operation of these converters can prove to be widely useful. These converters see quite a many load changes in their operating lifetime. This means that it is crucial to have knowledge and control of the dynamic characteristics of these converters, such as response time and droop. Reducing the magnitude of droop and decreasing response times can improve the reliability

of loads connected to these converters, and in rare cases even forestall brownout protection kicking in [6]. In essence, improvement of dynamic characteristics (including but not limited to droop and response time) lead to better operating conditions and better reliability. The objective for this thesis is to improve the dynamic characteristics and stability of DC-DC boost converters in demanding applications. The primary focus is on reducing the transition time from one steady state to another, for step changes in load.

Pulsed power loads are getting more prevalent due to applications like electromagnetic aircraft launch systems (EMALS), lasers and radar systems on electric ships [7][8][9]. Pulsed power loads cause stability issues for systems they are deployed in [10][11][12]. Improvements in stability margins would help in running higher power levels for such loads or similar power levels with higher ON times. Thus, any improvement in stability margins using a different control technique and/or topology is very desirable. The second objective for this thesis is to attempt to improve the stability margins for pulsed power loads.

1.2 Background

The transition time from one steady state to another in a converter can be minimized by taking advantage of the nonlinearity in the magnetics' saturation [13][14]. Inductor

cores behave nonlinearly and are saturating by nature [15]. Thus, this improvement in transition time is brought about by an improvement in the accuracy of the model. It has also been shown that using bang-bang control for specific time intervals can minimize the transition time from one steady state to another [16][17]. The nonlinear saturating inductor model when used with this bang-bang control strategy yields a significant improvement in transition time (2.92 times faster) when compared to the linear model of an inductor, albeit at the cost of higher transient values [13]. An interesting detail to make note of is that even though the higher value of transients lead to higher peak power losses, the significantly shorter transition duration makes the total energy loss lower. These results provoke a thought: Can the transition time be further improved by finding a way to push the inductor core towards saturation faster than usual? These results also show that the application of bang-bang control in conjunction with the nonlinear saturating inductor model has only been done on step increase in loads. This poses a twofold question: Can a similar bang-bang technique be used for step decrease in loads, and can anything be changed in a typical boost converter's topology to improve this? This thesis attempts to answer these questions.

Researchers have re-defined stability for pulsed power loads to be meta-stable [7][18], because a period of instability where the bus voltage grows without any bounds followed by a period of stability where the bus voltage oscillations dampen, keep the voltage within the bounds of stability. Thus, systems that are able to keep their states within the bounds of stability over periodic intervals of instability and

stability are classified to be meta-stable. For a pulsed power load whose power level, time period of the pulse and duty cycle of the pulse can be varied, a map for the meta-stability margins can be created using Hamiltonian Surface Shaping Power Flow Control (HSSPFC) over a wide range of parameters [7]. In essence, if the system is generating more energy than it is dissipating over one limit cycle, the system will grow beyond the bounds of stability and become unstable, and if the system is dissipating more energy than it is generating over one limit cycle, the system will remain within the bounds of stability and is stable (or meta-stable to be precise) [7][19]. Floquet theory is used for analyzing systems described by periodic linear differential equations [20][21][22]. Periodic nonlinear systems can be linearized around their operating point [23], and then can be analyzed using Floquet theory. Stability margins computed for pulsed power loads using this technique, when compared to the margins computed for the nonlinear system using HSSPFC show that Floquet analysis yields higher margins with certain details missing [7]. This means that Floquet analysis may point to the system being inside the bounds of stability even though it may not be. The reason for this is the fact that Floquet analysis uses the linearized system instead of the full nonlinear system model. An important point to note here is the fact that all previous research to map the meta-stability margins uses the linear inductor model with constant duty cycle control. This poses an important question - can the meta-stability margins be improved by applying bang-bang control in conjunction with any other topology improvements made in this thesis?

Taking a look at the previous research into modeling and analysis of coupled inductors is important, because they play an important part in the proposed solution in this thesis. In most cases where coupled inductors are used, linear models of inductance and mutual inductance are used to describe the dynamics of the coupled inductors [24][25][26]. The magnetic properties of inductor cores are not taken into account while modeling the coupled inductor. When the magnetics of the inductor core are considered while modeling the coupled inductors, even then the core is assumed to be operating in the linear magnetic region [27][28][29]. This presents an opportunity to build a coupled inductor model that incorporates a nonlinear anhysteretic saturating inductor core model [13][30][31].

1.3 Thesis Overview

Chapter 2 presents the mathematical models used in current literature. It showcases two models - boost converter with a linear inductor, and boost converter with a nonlinear saturating inductor. In Chapter 3, a solution is proposed for the questions posed in the previous section of this chapter (Chapter 1), pertaining to whether the inductor's core can be pushed towards saturation faster than usual and whether any topology modifications can be made to improve dynamic characteristics for step changes in load. A mathematical model is derived from this proposed solution. This mathematical model is used in subsequent chapters to simulate different scenarios.

All simulations are conducted through Wolfram Mathematica [32]. Chapter 4 uses the bang-bang control technique for a step increase in load for a typical boost converter with a nonlinear saturating inductor model [13][17]. This is to emulate the results shown in previous research. Then a similar bang-bang control strategy is applied to the new topology derived in Chapter 2, and their results are compared with respect to a few key performance metrics. This chapter also applies bang-bang control for a step decrease in load for a typical boost converter with a nonlinear saturating inductor model. Then a similar bang-bang control strategy for a similar scenario to the new boost converter topology is presented. The results for the two are compared. Then Chapter 4 focuses on pulsed power loads. It compares the stability maps for pulsed power loads. The comparison is between the previously used topology and control technique, and the new topology with bang-bang control. The final chapter (Chapter 5) summarizes the conclusions from the results seen in the previous chapters. This chapter also includes a summary of what work can be done in the future to carry this research forward.

Chapter 2

Mathematical models of converters

2.1 Introduction

This chapter showcases the mathematical models for boost converters that are widely used for analysis in current literature. These models have completely different assumptions about how the inductor core's magnetics behave. Some brief information about these underlying assumptions of magnetic behavior in the inductor cores on which the models are based, is also given.

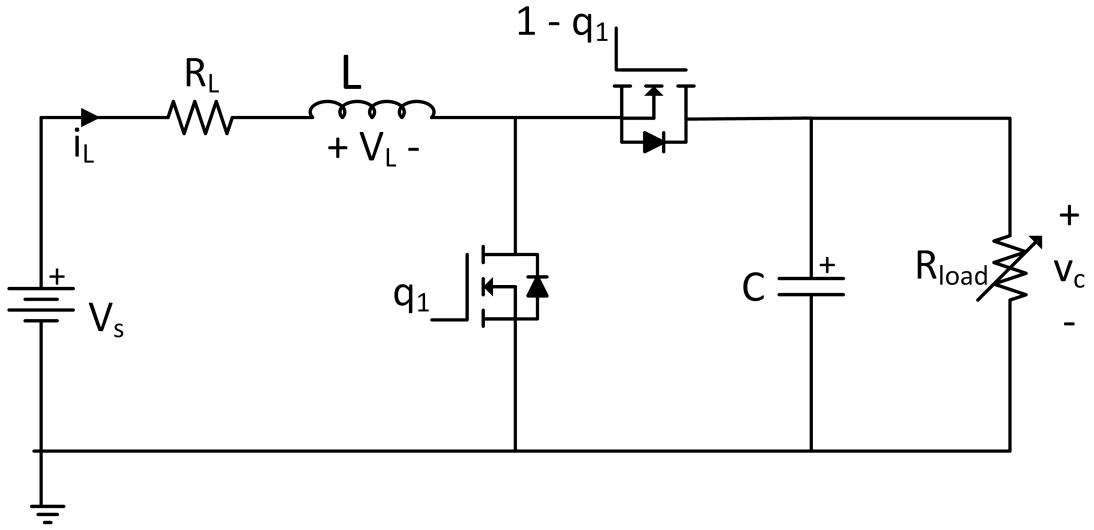

Figure 2.1: Boost converter with a linear inductor

2.2 Boost converter with a linear inductor

The model for the boost converter with a linear inductor is widely used for simulations and analyses pertaining to boost converters [33]. As the name suggests, the linear inductor model is used in the mathematical model. The linear inductor model is based on the assumption that there is no limit to the amount of flux that can flow through the inductor's core. The model for the boost converter with a linear inductor is shown in Figure 2.1. The model for the converter shown in Figure 2.1 is

$$L\,\frac{di_L}{dt} = V_s - i_L R_L - (1 - q_1)v_c \tag{2.1}$$

$$C\,\frac{dv_c}{dt} = (1 - q_1)i_L - \frac{v_c}{R_{load}} \tag{2.2}$$

where, V_s is the source voltage, i_L is the current flowing through the inductor, R_L is the parasitic resistance of the inductor, v_c is the capacitor voltage, q_1 is the switch state for the MOSFET labeled '1', C is the capacitance, L is the inductance, and R_{load} is the load resistance [13].

2.3 Boost converter with a nonlinear saturating inductor

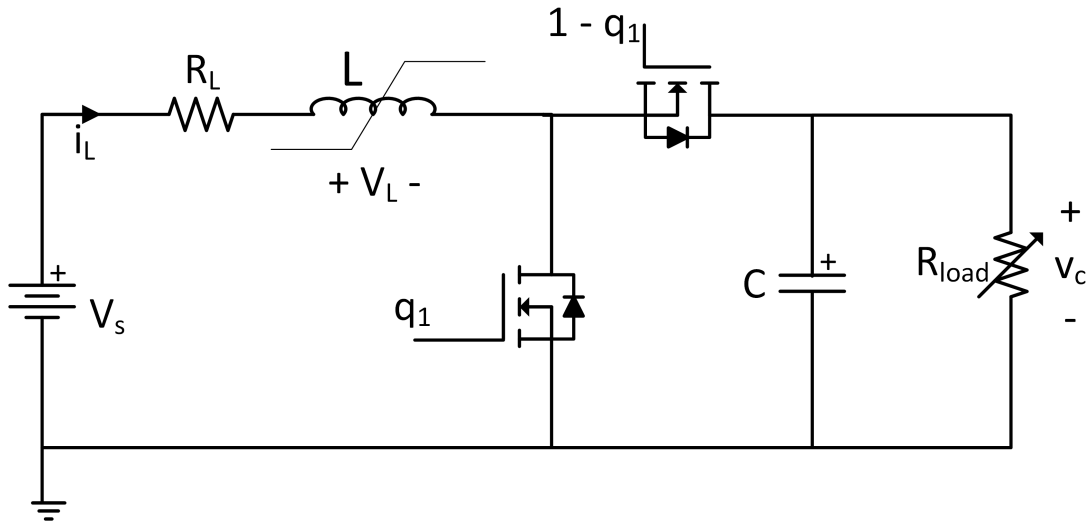

Figure 2.2: Boost converter with a nonlinear saturating inductor

The model for the boost converter with a nonlinear saturating inductor was developed by researchers to minimize transition time between steady states for step changes in load by utilizing bang-bang control [13]. The inductor core model in this boost converter is based on the fact that there is a limit to the amount of flux that can flow

through the inductor core and that it can get saturated. The model for the boost converter with a nonlinear saturating inductor is shown in Figure 2.2. The model for the converter shown in Figure 2.2 is

$$\frac{d\lambda}{dt} = V_s - i_L R_L - (1 - q_1) v_c \tag{2.3}$$

$$C \frac{dv_c}{dt} = (1 - q_1) i_L - \frac{v_c}{R_{load}} \tag{2.4}$$

$$\frac{\lambda}{N} = A_c \, a \, \arctan\left(b \frac{N \, i_L}{l_c} \right) \tag{2.5}$$

where, λ is the flux linkage of the inductor coil, V_s is the source voltage, i_L is the current flowing through the inductor, R_L is the parasitic resistance of the inductor, v_c is the capacitor voltage, q_1 is the switch state for the MOSFET labeled '1', C is the capacitance, L is the nominal inductance, R_{load} is the load resistance, a and b are material dependent constants, A_c is the cross sectional area of the inductor core, l_c is the effective magnetic path length of the inductor core, N are the turns in the coil that forms the inductor [13]. In subsequent chapters, these models will be used as the reference for previously researched models.

Chapter 3

Boost converter with a coupled inductor and bleed off resistor

3.1 Proposed solution

In Chapter 1, questions were posed about improving the dynamic characteristics of boost converters. In one of those questions it was mentioned that, an attempt to decrease the transition time can be made by finding a way to saturate the inductor core faster. This cultivated the idea to use a coupled inductor to achieve the goal of saturating the inductor core faster. The first coil performs the duties of an inductor, like in any typical boost converter. The sole purpose of the second coil is to saturate

the inductor core. Looking at this from a different perspective, for a step increase in load, the energy stored in a boost converter at steady state increases [34]. The second coil of the coupled inductor speeds up this process by adding energy in the form of magnetic flux. For a step decrease in load, it can be said that the energy stored in the converter at steady state decreases. This means that during the transition time between two steady states, the converter loses a portion of the energy stored in it. This plainly points to the idea that this process can be expedited by finding a way to burn this energy off posthaste. This can be achieved using a bleed-off resistor at the output capacitor. Thus, to achieve the objectives outlined in the previous chapter, a coupled inductor is added to assist with step increase in loads, and a bleed off resistor (high power resistor at the output) is added to assist with step decrease in loads. The boost converter model for this new topology can be seen in Figure 3.1. Also, a detailed model of the coupled inductor is shown in Figure 3.2.

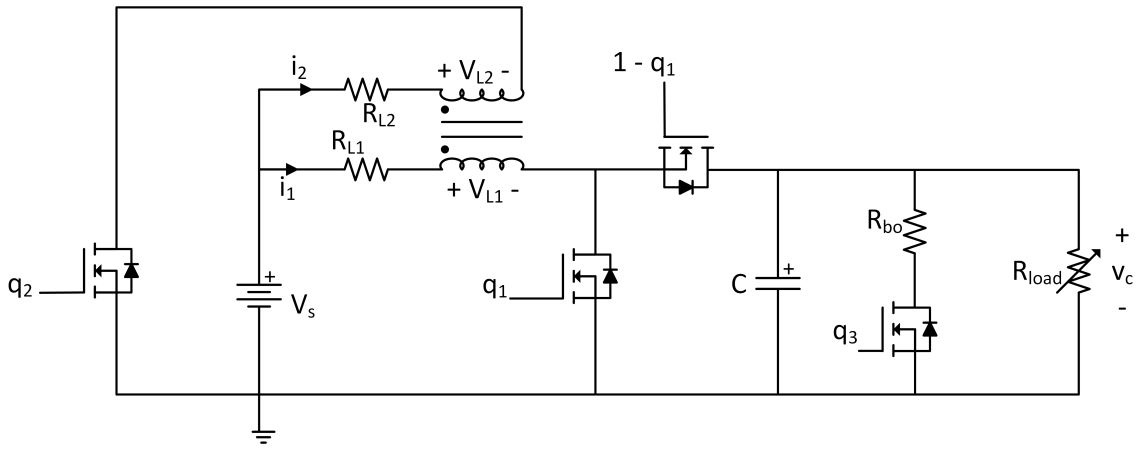

Figure 3.1: Boost converter with a coupled inductor and a bleed off resistor

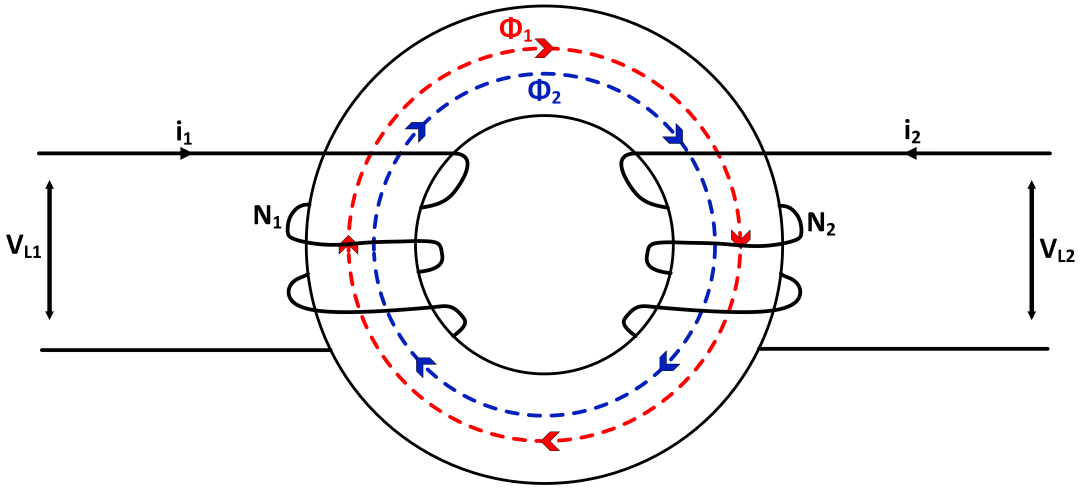

Figure 3.2: Coupled inductor

3.2 Mathematical modeling

There are two major parts to the derivation of the mathematical model for the converter seen in Figure 3.1. The first part is derived from the electrical circuit analysis of the converter shown in that figure, and the second part is derived from the magnetic circuit analysis of the coupled inductor shown in Figure 3.2. Applying Kirchhoff's Voltage Law (KVL) and Kirchhoff's Current Law (KCL) to the converter shown in Figure 3.1, results in

$$V_{L_1} = V_s - i_1 R_{L_1} - (1 - q_1) v_c \tag{3.1}$$

$$i_2 = q_2 \left(\frac{V_s - V_{L_2}}{R_{L_2}} \right) \tag{3.2}$$

$$C \frac{dv_c}{dt} = (1 - q_1) i_1 - q_3 \left(\frac{v_c}{R_{bo}} \right) - \frac{v_c}{R_{load}} \tag{3.3}$$

where, V_{L_1} is the voltage across the first coil, V_{L_2} is the voltage across the second coil, V_s is the source voltage, v_c is the voltage across the capacitor, C is the capacitance, R_{L_1} is the parasitic resistance of the first coil, R_{L_2} is the parasitic resistance of the second coil, q_1 is the switch state for the MOSFET labeled '1', q_2 is the switch state for the MOSFET labeled '2', q_3 is the switch state for the MOSFET labeled '3', i_1 is the current flowing through the first coil, i_2 is the current flowing through the second coil, R_{load} is the load resistor, and R_{bo} is the bleed off resistor. Analyzing the core of the coupled inductor shown in Figure 3.2, and assuming the total flux produced by the two coils contributes towards saturating the inductor core i.e. no flux leakage, it can be said that

$$\phi_1 + \phi_2 = \phi_{total} \tag{3.4}$$

where, ϕ_1 is the flux created by the current in the first coil, ϕ_2 is the flux created by the current in the second coil, and ϕ_{total} is the total flux in the inductor core. The relationships between the fluxes and self flux linkages for the two coils in the coupled inductor are

$$\lambda_{11} = \phi_1 \, N_1 \tag{3.5}$$

$$\lambda_{22} = \phi_2 \, N_2 \tag{3.6}$$

where, λ_{11} is the self flux linkage of the first coil, λ_{22} is the self flux linkage of the second coil, N_1 are the number of turns in the first coil, and N_2 are the number of turns

in the second coil. Rearranging equation (3.5) and equation (3.6) and substituting them in equation (3.4) results in

$$\frac{\lambda_{11}}{N_1} + \frac{\lambda_{22}}{N_2} = \phi_{total}. \tag{3.7}$$

The magnetic flux density in the inductor's core denoted by B can be expressed as

$$B = \frac{\phi_{total}}{A_c} \tag{3.8}$$

where, A_c is the cross-sectional area of the inductor's core. Rearranging equation (3.8) and substituting it in equation (3.7) results in

$$\frac{\lambda_{11}}{N_1} + \frac{\lambda_{22}}{N_2} = A_c\, B. \tag{3.9}$$

The $B-H$ curve for a material where the magnetic field intensity is denoted by H, assuming nonlinear anhysteretic behavior is

$$B = a\ \arctan(b\, H) \tag{3.10}$$

where, a and b are material dependent constants [13]. Substituting equation (3.10) in equation (3.9) results in

$$\frac{\lambda_{11}}{N_1} + \frac{\lambda_{22}}{N_2} = A_c\, a\ \arctan(b\, H). \tag{3.11}$$

Magnetic fields can be superimposed and added linearly if their orientation is in the same direction [35]. The magnetic fields produced by the two coils shown in Figure 3.2 can be added, as their fields will be aligned inside the inductor's core. Using this phenomenon, equation (3.11) becomes

$$\frac{\lambda_{11}}{N_1} + \frac{\lambda_{22}}{N_2} = A_c\, a\, \arctan(b\,(H_1 + H_2)) \tag{3.12}$$

where, H_1 is the H-field created by the current flowing through the first coil and H_2 is the H-field created by the current flowing through the second coil. H fields created by both coils are expressed as

$$H_1 = \frac{N_1\, i_1}{l_c} \tag{3.13}$$

$$H_2 = \frac{N_2\, i_2}{l_c} \tag{3.14}$$

where, l_c is the effective magnetic path length of the inductor's core. Substituting equation (3.13) and equation (3.14) in equation (3.12) results in

$$\frac{\lambda_{11}}{N_1} + \frac{\lambda_{22}}{N_2} = A_c\, a\, \arctan\left(b\,\left(\frac{N_1\, i_1}{l_c} + \frac{N_2\, i_2}{l_c}\right)\right). \tag{3.15}$$

If it is assumed that the above equation has two unknowns in λ_{11} and λ_{22}, another equation is required for a unique solution. The second equation can be derived with a simple thought experiment. If the fluxes of the two coils in question were opposing

each other, the equation would largely remain the same but the two addition operators would be replaced by two subtraction operators. This is expressed as

$$\frac{\lambda_{11}}{N_1} - \frac{\lambda_{22}}{N_2} = A_c\, a\, \arctan\left(b\, \left(\frac{N_1\, i_1}{l_c} - \frac{N_2\, i_2}{l_c}\right)\right). \tag{3.16}$$

The coefficient of coupling denoted by k is assumed to be less than one. Thus, from each coil's perspective, only k times the flux produced by the other coil is going to interact with it. Thus, the total flux linkages for each of the coils are

$$\lambda_1 = N_1\, (\phi_1 + k\, \phi_2) \tag{3.17}$$

$$\lambda_2 = N_2\, (\phi_2 + k\, \phi_1) \tag{3.18}$$

where, λ_1 is the flux linkage of the first coil and λ_2 is the flux linkage of the second coil. Rewrite these equations as

$$\lambda_1 = N_1\, \phi_1 + \frac{k\, N_1\, N_2\, \phi_2}{N_2} \tag{3.19}$$

$$\lambda_2 = N_2\, \phi_2 + \frac{k\, N_2\, N_1\, \phi_1}{N_1}. \tag{3.20}$$

Using equations (3.5) and (3.6) to simplify equations (3.19) and (3.20) results in

$$\lambda_1 = \lambda_{11} + \frac{k\, N_1\, \lambda_{22}}{N_2} \tag{3.21}$$

$$\lambda_2 = \lambda_{22} + \frac{k\, N_2\, \lambda_{11}}{N_1}. \tag{3.22}$$

The relationships between voltages across the inductor coils and the flux linkages are

$$V_{L_1} = \frac{d\lambda_1}{dt} \tag{3.23}$$

$$V_{L_2} = \frac{d\lambda_2}{dt}. \tag{3.24}$$

Differentiating both sides of (3.21) and (3.22), and using the relationships given above results in

$$V_{L_1} = \frac{d\lambda_{11}}{dt} + k\,\frac{N_1}{N_2}\frac{d\lambda_{22}}{dt} \tag{3.25}$$

$$V_{L_2} = \frac{d\lambda_{22}}{dt} + k\,\frac{N_2}{N_1}\frac{d\lambda_{11}}{dt}. \tag{3.26}$$

Solving these equations simultaneously results in

$$\frac{d\lambda_{11}}{dt} = \frac{N_2\,V_{L_1} - k\,N_1\,V_{L_2}}{(1-k^2)N_2} \tag{3.27}$$

$$\frac{d\lambda_{22}}{dt} = \frac{N_1\,V_{L_2} - k\,N_2\,V_{L_1}}{(1-k^2)N_1}. \tag{3.28}$$

Aggregating all the relevant equations - (3.1), (3.2), (3.3), (3.15), (3.16), (3.27) and (3.28) - the mathematical model is

$$V_{L_1} = V_s - i_1 R_{L_1} - (1 - q_1) v_c \tag{3.29}$$

$$i_2 = q_2 \left(\frac{V_s - V_{L_2}}{R_{L_2}} \right) \tag{3.30}$$

$$C \, \frac{dv_c}{dt} = (1 - q_1) i_1 - q_3 \left(\frac{v_c}{R_{bo}} \right) - \frac{v_c}{R_{load}} \tag{3.31}$$

$$\frac{\lambda_{11}}{N_1} + \frac{\lambda_{22}}{N_2} = A_c \, a \, \arctan \left(b \, \left(\frac{N_1 \, i_1}{l_c} + \frac{N_2 \, i_2}{l_c} \right) \right) \tag{3.32}$$

$$\frac{\lambda_{11}}{N_1} - \frac{\lambda_{22}}{N_2} = A_c \, a \, \arctan \left(b \, \left(\frac{N_1 \, i_1}{l_c} - \frac{N_2 \, i_2}{l_c} \right) \right) \tag{3.33}$$

$$\frac{d\lambda_{11}}{dt} = \frac{N_2 \, V_{L_1} - k \, N_1 \, V_{L_2}}{(1 - k^2) N_2} \tag{3.34}$$

$$\frac{d\lambda_{22}}{dt} = \frac{N_1 \, V_{L_2} - k \, N_2 \, V_{L_1}}{(1 - k^2) N_1}. \tag{3.35}$$

The mathematical model shown above has seven states and is a Differential-Algebraic system of Equations (DAEs), and Wolfram Mathematica uses the IDA method developed by the Center for Applied Scientific Computing at the Lawrence Livermore National Laboratory to solve DAEs [36][37][38]. An important point to note is that the above given mathematical model can only be used when the second coil is switched ON. When the second coil is switched OFF, the coupled inductor behaves like a normal inductor albeit with a nonlinear saturating inductor model. This means that the above model has to be modified to be the same as the converter model seen in

previous research [13], except for the addition of the bleed off resistor. This model is

$$\frac{d\lambda_1}{dt} = V_s - i_1 R_{L_1} - (1 - q_1) v_c \tag{3.36}$$

$$C\,\frac{dv_c}{dt} = (1 - q_1) i_1 - q_3 \left(\frac{v_c}{R_{bo}} \right) - \frac{v_c}{R_{load}} \tag{3.37}$$

$$\frac{\lambda_1}{N_1} = A_c\, a\, \arctan\left(b\, \frac{N_1\, i_1}{l_c} \right). \tag{3.38}$$

A key point must be noted in the mathematical model given above. As the second coil is OFF, the self flux linkage for the first coil is the same as the total flux linkage for the first coil. This topology also contains an interesting phenomenon. The flux in an inductor core cannot change instantaneously. Thus, when the second coil is switched OFF, all the flux in the inductor core can only interact with the first coil. This causes a jump in the current flowing through the first coil, when the switching event occurs. Assuming a lossless transfer of energy, the value of the current through the first coil right after the jump can be calculated as

$$i_1 = \frac{l_c}{b\, N_1}\, \tan\left(\frac{1}{A_c\, a}\, \left(\frac{\lambda_{11}}{N_1} + \frac{\lambda_{22}}{N_2} \right) \right). \tag{3.39}$$

This relationship is derived from (3.32) and the fact that the current through the second coil falls to zero when the second coil is switched OFF. This discontinuity must be modeled into simulations. Another factor that must be modeled into simulations is the energy loss during transition. Calculating the energy losses during transition is important to compare the wasted energy between two different techniques. The

energy loss will be through the parasitic resistance of the coils and the bleed off resistor [39][40][41]. This assumes all other circuit elements to be ideal. Thus, the energy loss during transitions can be calculated as

$$E_{loss} = \int_{t_1}^{t_2} \left(i_1^2 R_{L_1} + i_2^2 R_{L_2} + q3 \left(\frac{v_c^2}{R_{bo}} \right) \right) dt \tag{3.40}$$

where, E_{loss} is the transition energy loss, t_1 is the time at which the transition begins, and t_2 is the time at which the transition ends. In the mathematical model presented above, the turns in the inductor coil denoted by N is used as a parameter, although the inductance denoted by L is the parameter chosen during the design phase. Thus, the number of turns in the inductor coil need to be calculated for that given inductance. These turns are calculated as

$$N = \sqrt{\frac{L_{nominal}\, l_c}{a\, b\, A_c^2}} \tag{3.41}$$

where, $L_{nominal}$ is the nominal inductance of the coil in question [13]. In this thesis, the inductor core is modeled after the Mix-52 material from the Micrometals' catalogue [42]. The specific part number is T650-52. Parameters for the model developed in this chapter for the T650-52 part are also seen in previous research [13]. These parameters are listed in Table 3.1, and will be used for all simulations in this thesis here on out.

In summary, the mathematical model for this topology contains two sets of state

Table 3.1
Inductor core parameters for T650-52

Parameter	Value
A_c	$0.00184m^2$
l_c	$0.399m$
a	1.0237875
b	0.0002189

equations, one set for when the second coil of the coupled inductor is switched ON and one set for when it is switched OFF. The model also contains a third important element, the discontinuity caused in the current through the first coil due to the switching event of the second coil being switched OFF. This topology will be referred to as the CIBR boost converter (Coupled Inductor - Bleed off Resistor boost converter) here on out in this thesis. In subsequent chapters, the CIBR topology in conjunction with bang-bang control will be used to compare against the models and techniques used in previous research.

Chapter 4

Applications and demonstration

4.1 Introduction

The previous chapter proposes a solution to achieve the objectives outlined in the first chapter of this thesis and derives the mathematical model for this solution. In this chapter, the CIBR topology in conjunction with bang bang control will be applied to different test scenarios for the load, and the behavior of the converter will be demonstrated through simulations. The transition processes for step increase and step decrease in resistive loads are presented and compared to the transition processes for the same with the old topology. These transition processes for the CIBR topology can be applied to pulsed power loads, as they can be seen as a series of step changes in

load, albeit the load is a power load and not a resistive load. Then the meta-stability margins are examined and compared to the margins computed with the old topology.

4.2 Minimum time response for a step increase in resistive load

This section shows the response of a boost converter with a nonlinear saturating inductor and a CIBR boost converter with bang-bang control for a step increase in load. In the first subsection, the transition process for a boost converter with a nonlinear saturating inductor is demonstrated with simulation. In the second subsection, the transition process for a CIBR boost converter is demonstrated with simulation. The third and final subsection compares these transitions and shows what improvements can be had with a CIBR boost converter.

4.2.1 Transition process for a boost converter with a nonlinear saturating inductor

The transition is based on previous research that uses bang-bang control for minimizing transition time [17]. For a step increase in load, the boost converter with

a nonlinear saturating inductor transitions from one steady state to another in two phases. The transition process is an open loop process and the timings are pre-calculated. In the first phase of the transition, the switch 'q1' is ON for a certain time interval. The end of this time interval marks the end of the first phase of this transition and the beginning of the second phase of the transition. In the second phase of this transition, the switch 'q1' is switched OFF for another specific time interval. The end of this second time interval marks the end of the second phase of the transition, and thus marks the end of the transition process. The converter now reverts back to duty cycle control. The time intervals for the transition phases can be found by minimizing the sum of square errors of the inductor current and output voltage for the forward time trajectories of the system (where 'q1' is ON) and the backward time trajectories of the system (where 'q1' is OFF).

$$\min J(t_f, t_r) = (v_c(t_f) - v_c(t_r))^2 + (i_L(t_f) - i_L(t_r))^2 \tag{4.1}$$

where, J is the cost function, t_f is the forward time, t_r is the reverse time, $v_c(t_f)$ and $i_L(t_f)$ represent the forward time trajectories, and $v_c(t_r)$ and $i_L(t_r)$ represent the reverse time trajectories. The initial values of the forward time trajectories are the state values just before the transition occurs, and the initial values of the backward time trajectories can be taken from the steady state of the new load. The values for t_f and t_r that minimize the cost function are the required time intervals. The parameters used to conduct the simulation to demonstrate the transition process use

the values shown in Table 4.1.

Table 4.1
Parameters for simulating a step increase in load for a boost converter with a nonlinear saturating inductor

Parameter	Value
V_s	200 V
R_L	1 $m\Omega$
$L_{nominal}$	1 mH
N	32
C	1 mF
$R_{load,1}$	32 Ω
$R_{load,2}$	8 Ω
$f_{sw,q1}$	10 kHz
$v_{c,ref}$	400 V

The step change in load is

$$R_{load} = \begin{cases} R_{load,1} & t < 0.0005 \\ R_{load,2} & \text{otherwise} \end{cases} \tag{4.2}$$

where, R_{load} is the load connected to the converter, $R_{load,1}$ is the value of the load before the transition, and $R_{load,2}$ is the value of the load after the transition. The plots for the results of the simulation of the transition process can be seen in Figure 4.1 and Figure 4.2. Figure 4.1 shows the inductor current and Figure 4.2 shows the capacitor voltage. The two phases of the transition process can be seen in both plots. Important performance metrics logged in the simulation are given in Table 4.2.

Table 4.2
Performance metrics from the simulation of a step increase in load for a boost converter with a nonlinear saturating inductor

Performance metric	Value
Transition time	412.002 μs
Peak i_L	355.088 A
Minimum v_c	385.242 V
Energy loss during transition	8.89408 mJ

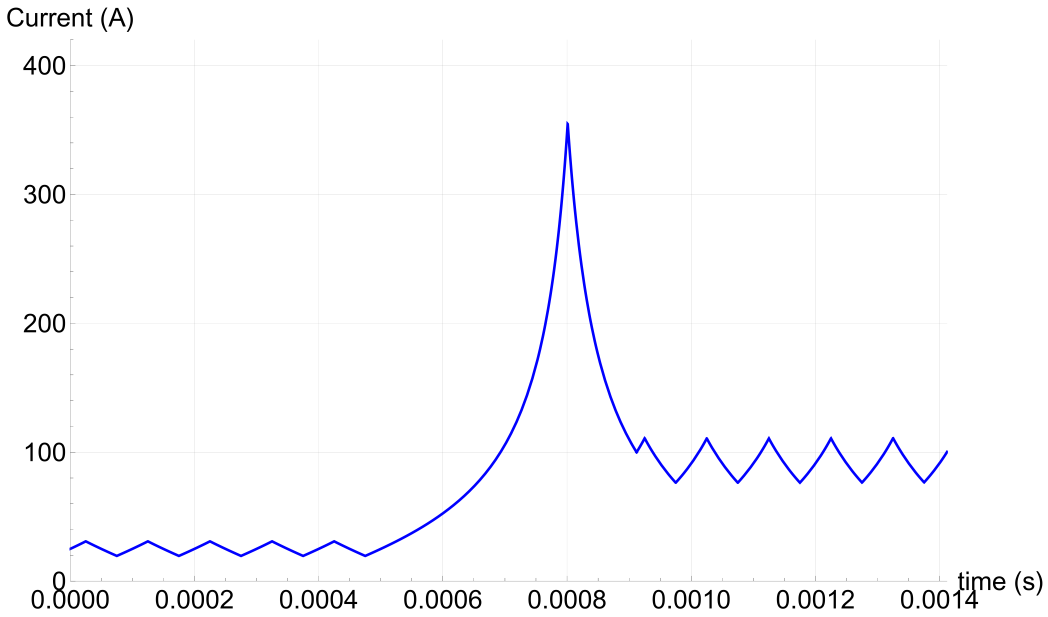

Figure 4.1: Inductor current in the boost converter with a nonlinear saturating inductor for a step increase in load

4.2.2 Transition process for a CIBR boost converter

The transition is largely based on previous research that uses bang-bang control for minimizing transition time [17]. The control law used here is conceptually similar. The modifications made in the CIBR topology only augment the control law, not

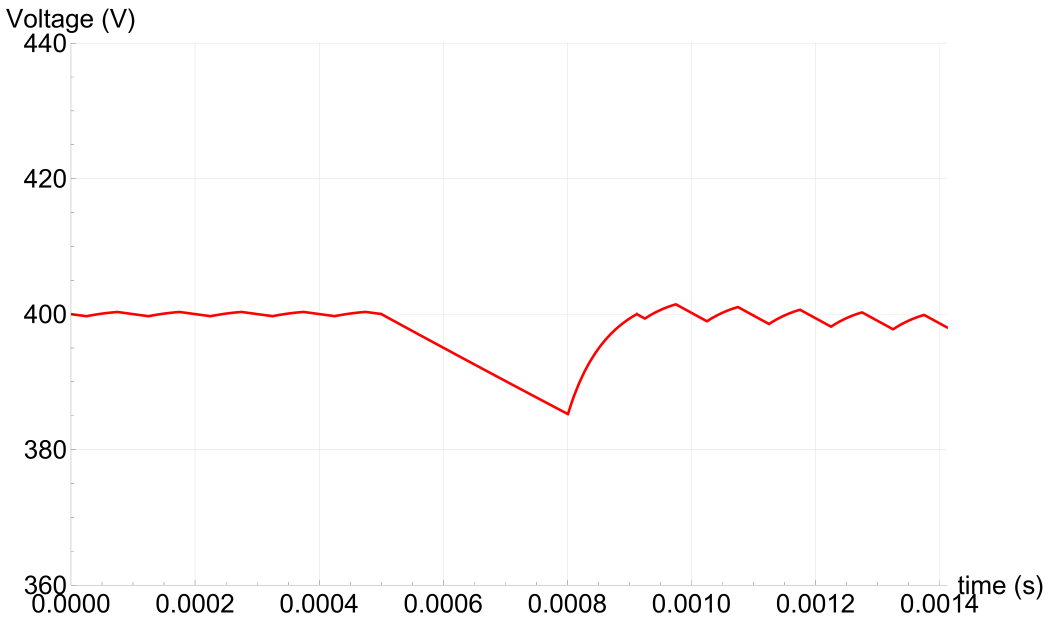

Figure 4.2: Capacitor voltage in the boost converter with a nonlinear saturating inductor for a step increase in load

fundamentally change it. For a step increase in load for a CIBR boost converter, the control strategy helps the converter transition in three phases. This is an open loop process and all required timings are pre-calculated. In the first phase, the second coil of the coupled inductor is pre-charged. This pre-charging process happens before the load transitions. During this phase, the second coil of the coupled inductor is switched ON and the first coil uses a high constant duty cycle. When the second coil is ON, some of the flux generated by the first coil helps to increase the current in the second coil. This would have caused a drop in the current through the first coil would it not have been for the high duty cycle. This high duty cycle can be selected arbitrarily, provided it is high enough to keep the current from dropping off. In this thesis, it is set at 89%. The pre-charging time affects the performance of the next phases of the

transition. An increase in pre-charging time leads to an increase in the initial value of the current in the second coil for the next phase of the transition. Although this is a good thing to decrease the transition time, a big increase in pre-charging time may cause a noticeable drop in the output voltage, which is an undesirable effect. To make sure the output voltage drop remains negligible, a balance must be struck between the pre-charging time and the allowable voltage drop. The pre-charging process is set up in such a way that the final value of the current in the second coil is equal to the initial value of the current in the first coil. This means that the final values of the currents in both coils are the same. This assumes no drop in the current in the first coil, and no drop in the output voltage beyond a couple of percentage points of the nominal ripple. If the voltage drop limit of two percent beyond the nominal ripple is breached, the pre-charging process is set up to enforce the voltage limit instead of trying to make the final value of the current in the second coil equal to the initial value of the current in the first coil. To find the initialization time (time taken for pre-charging), the forward time system (where 'q1' is at a arbitrarily high duty cycle and 'q2' is ON) is simulated until either the current in the second coil is equal to the initial value of the current in the first coil, or the capacitor voltage breaches and falls beyond the threshold voltage. The initial values for this simulation are the steady

state values at the load the converter is transitioning from.

$$t_i = \begin{cases} t_{i1=i2} & \text{if } vc_f \geq vc_{threshold} \\ t_{vc} & \text{if } vc_f < vc_{threshold} \end{cases} \tag{4.3}$$

where, t_i is the initialization time i.e. time taken for the pre-charging process, $t_{i1=i2}$ is the time at which the current through the second coil becomes equal to the initial value of the current through the first coil, t_{vc} is the time at which the capacitor voltage falls just below the threshold voltage, vc_f is the value of the capacitor voltage at time $t_{i1=i2}$, and $vc_{threshold}$ is the value of the threshold voltage (here, the threshold is 2% beyond the nominal ripple). The end of the pre-charging process marks the end of the first phase and the beginning of the second phase of the transition process. During the second phase, both coils are ON. After a certain time interval, both coils are switched OFF. This marks the end of the second phase and the beginning of the third phase of the transition. In the third phase of the transition, both coils are OFF for a specific time interval. At the end of the third phase of the transition (also the end of the transition), which is marked by the end of the time interval mentioned previously, the converter reverts to a closed loop duty cycle control strategy. The time intervals for the second and third phases of the transition can be found by minimizing the sum of the square errors for core flux and output voltage from the forward time trajectories of the system (where 'q1' and 'q2' are ON) and the reverse time trajectories of the

system (where 'q1' and 'q2' are OFF).

$$\min J(t_f, t_r) = (v_c(t_f) - v_c(t_r))^2 + w\left(\frac{\lambda_{11}(t_f)}{N_1} + \frac{\lambda_{22}(t_f)}{N_2} - \frac{\lambda_1(t_r)}{N_1}\right)^2 \tag{4.4}$$

where, J is the cost function, t_f is the forward time, t_r is the reverse time, $v_c(t_f)$, $\lambda_{11}(t_f)$ and $\lambda_{22}(t_f)$ represent the forward time trajectories, $v_c(t_r)$ and $\lambda_1(t_r)$ represent the reverse time trajectories, and w is the weighting factor applied to the flux trajectories. The initial values for the forward time trajectories are the final values seen at the end of the pre-charging process, and the initial values for the reverse time trajectories are taken from the desired operating point of the system at the new load. The values for t_f and t_r that minimize the cost function are the required time intervals. An important factor to note is that the flux trajectories have to be weighted in such a way that their average values are comparable to the average values of the output voltage trajectories to neutralize the heavy bias towards the output voltage trajectories, which exists by virtue of their values being considerably higher. Another factor to keep note of in this scenario is the use of the flux trajectories to find the time intervals instead of the current trajectories. The reason for this is the current jump phenomenon seen in the CIBR boost converter topology. The flux on the other hand does not change instantaneously. This makes using the total flux trajectories (whose values do not jump) to find the second and third phase time intervals feasible, compared to using the current trajectories. The parameters used to conduct the simulation to demonstrate this transition process use the values shown in Table 4.3.

Table 4.3
Parameters for simulating a step increase in load for a CIBR boost converter

Parameter	Value
V_s	200 V
R_{L_1}	1 $m\Omega$
R_{L_2}	1 $m\Omega$
$L_{1,nominal}$	1 mH
N_1	32
$L_{2,nominal}$	1 mH
N_2	32
C	1 mF
R_{bo}	8 Ω
$R_{load,1}$	32 Ω
$R_{load,2}$	8 Ω
$f_{sw,q1}$	10 kHz
$v_{c,ref}$	400 V

The step change in load is

$$R_{load} = \begin{cases} R_{load,1} & t < 0.001 \\ R_{load,2} & \text{otherwise} \end{cases} \tag{4.5}$$

where, R_{load} is the load connected to the converter, $R_{load,1}$ is the value of the load before the transition, and $R_{load,2}$ is the value of the load after the transition. The plots for the results of the simulation of the transition process can be seen in Figures 4.3 through 4.6. Figure 4.3 shows the current through the first coil of the coupled inductor, Figure 4.4 shows the current through the second coil of the coupled inductor, Figure 4.5 shows the total flux in the coupled inductor core, and Figure 4.6 shows the capacitor voltage. The current jump phenomenon can be seen in the plot of the

current through the first coil. The pre-charging process can be seen in the plot of the current through the second coil. The plots show that t_i is very small and that the voltage drop during this phase is negligible. The second and third phases can be seen in Figure 4.6. Important performance metrics logged in the simulation are given in Table 4.4.

Table 4.4
Performance metrics from the simulation of a step increase in load for a CIBR boost converter

Performance metric	Value
Transition time	247.953 μs
Peak i_1	237.952 A
Minimum v_c	391.088 V
Energy loss during transition	3.33689 mJ

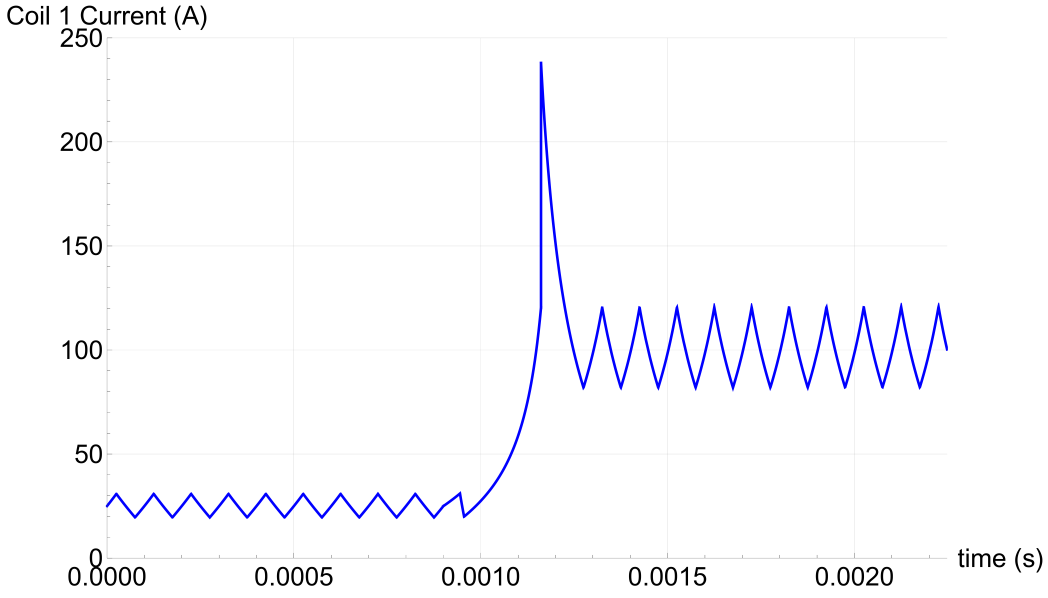

Figure 4.3: Current through the first coil of the CIBR boost converter for a step increase in load

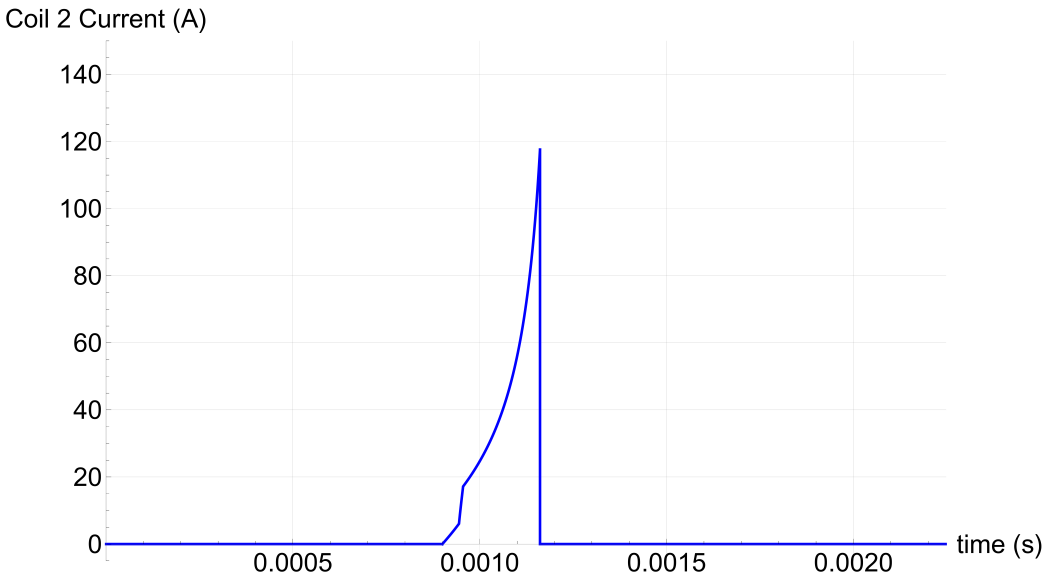

Figure 4.4: Current through the second coil of the CIBR boost converter for a step increase in load

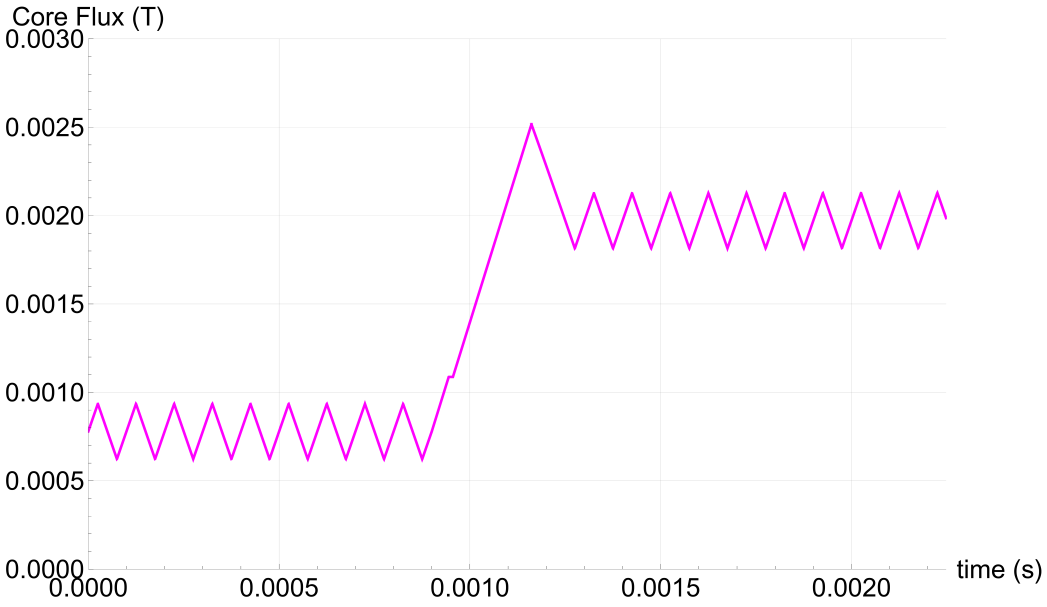

Figure 4.5: Total flux in the inductor core of the CIBR boost converter for a step increase in load

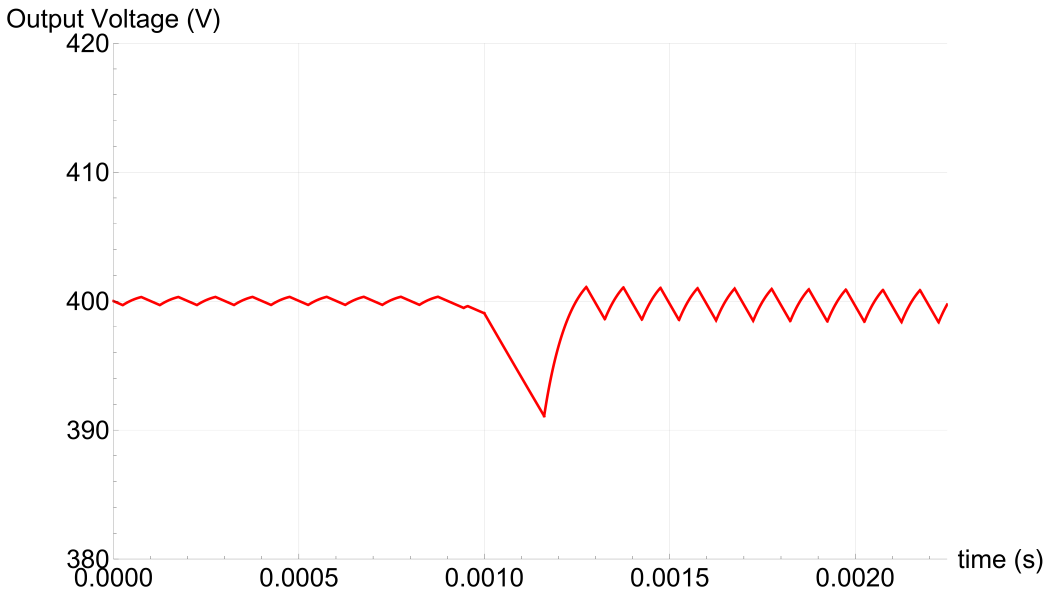

Figure 4.6: Capacitor voltage of the CIBR boost converter for a step increase in load

4.2.3 Comparison of the transition processes

Comparison of the CIBR boost converter and the boost converter with a nonlinear saturating inductor for a step increase in load can be seen in Table 4.5.

Table 4.5
Comparison between boost converter with a nonlinear saturating inductor and CIBR boost converter

Performance metric	Nonlin. sat. ind.	CIBR	Improvement
Transition time	412.002 μs	247.953 μs	39.8175%
Peak inductor current	355.088 A	237.952 A	32.9878%
Minimum voltage	385.242 V	391.088 V	1.5174%
Energy loss during transition	8.89408 mJ	3.33689 mJ	62.4819%

A reduction in transition time between steady states can be seen from the results

shown in Table 4.5. Even though the percentage improvement for minimum v_c isn't substantial, the reduction in the voltage drop in terms of magnitude is not negligible. On the other hand, the peak inductor current seen is considerably lower, which is a sound improvement. Even though there are two coils in play with a coupled inductor, due to the low peak values and considerably small transition time, the transition energy loss due to the parasitic resistance is considerably lower.

4.3 Minimum time response for a step decrease in resistive load

This section shows the response of a boost converter with a nonlinear saturating inductor and a CIBR boost converter with bang-bang control for a step decrease in load. The first subsection demonstrates via simulation the transition process for a boost converter with a nonlinear saturating inductor. The second subsection demonstrates via simulation the transition process for a CIBR boost converter. The third and final subsection compares these transitions and shows what improvements can be had with a CIBR boost converter.

4.3.1 Transition process for a boost converter with a nonlinear saturating inductor

The transition is largely based on previous research that uses bang-bang control for minimizing transition time [17]. In previous research, the control policy was only applied for step increases in load. To apply a similar control strategy for step decreases in load, the control law is kept conceptually the same, except the switch states are reversed. The transition process for a step down change in load for a boost converter with a nonlinear saturating inductor model can go one of two ways - the transition can be either in CCM (Continuous Conduction Mode) or in DCM (Discontinuous Conduction Mode). To check which mode is required, a small test needs to be conducted.

$$\text{Mode} = \begin{cases} \text{DCM} & \text{if } v_{tf} \geq v_{tb} \\ \text{CCM} & \text{if } v_{tf} < v_{tb} \end{cases} \tag{4.6}$$

where, v_{tf} is the value of the output voltage at the end of the forward-time simulation, and v_{tb} is the value of the output voltage at the end of the backward-time simulation. For the mode test, the forward-time system is simulated with the switch 'q1' OFF till the current reaches zero. The initial values of this simulation are the final values of the previous steady state at which the transition will begin. The backward-time system is simulated with the switch 'q1' ON till the current reaches zero, with the

initial values of the simulation being the desired operating point for the new load. If the value of the output voltage at the end of the forward-time simulation is higher than or equal to the output voltage at the end of the the backward-time simulation, the transition will be in DCM. If it is lower, the transition will be in CCM.

A CCM transition occurs in two phases. The transition in load marks the beginning of the first phase. In the first phase, the switch 'q1' is switched OFF for a specific time interval. The end of this time interval marks the end of the first phase and the beginning of the second phase of this transition process. In the second phase, the switch 'q1' is ON for a certain time interval. The end of this time interval marks the end of the second phase of the transition, and the end of the full transition process as well. Now, the system is expected to be at the desired operating point, which is the steady state operating point for the new load. The converter also reverts back to duty cycle control. The time intervals for the transition phases are crucial for this process to work. These time intervals can be computed by minimizing the sum of square errors of the inductor current and output voltage for the forward time trajectories of the system (where 'q1' is OFF) and the reverse time trajectories of the system (where 'q1' is OFF).

$$\min J(t_f, t_r) = (v_c(t_f) - v_c(t_r))^2 + (i_L(t_f) - i_L(t_r))^2 \tag{4.7}$$

where, J is the cost function, t_f is the forward time, t_r is the reverse time, $v_c(t_f)$

and $i_L(t_f)$ represent the forward time trajectories, and $v_c(t_r)$ and $i_L(t_r)$ represent the reverse time trajectories. Similar to the step increase in load transition process, the initial values of the forward time trajectories are the final values before the transition begins, and the initial values of the reverse time trajectories are derived from the required steady state of the new load. The values for t_f and t_r that minimize the cost function are the required time intervals.

A DCM transition occurs in three phases. As with the CCM transition process, the change in load marks the beginning of the first phase. In the first phase, the switch 'q1' is switched OFF till the current reaches zero. This marks the end of the first phase of the transition and the beginning of the second phase of the transition. In the second phase, 'q1' stays OFF till the output voltage falls to a certain value. This value is the final value of the output voltage for the reverse time trajectory from the mode test conducted to determine whether the transition process is in CCM or in DCM. This value of the output voltage is denoted as v_{tb} in the mode test. When the output voltage reaches this value, 'q1' is switched ON. This marks the end of the second phase and the beginning of the third phase of the transition. In the third and final phase of the transition process, 'q1' is ON for a specific time interval. At the end of this time interval, the states reach the desired operating point and the converter reverts back to duty cycle control. Here, t_{i0f} is the time taken by the current to reach zero in the forward time simulation. It also denotes the time interval for the first phase. t_{vtb} is the time taken by the output voltage to reach v_{tb} in the forward time simulation.

It also denotes the time interval for the second phase. t_{i0r} is the time taken by the current to reach zero in the reverse time simulation. It also denotes the time interval for the third phase. The time intervals for the DCM transition process are pretty straightforward to compute. The time interval for the first phase can be computed by finding the time required for the inductor current to reach zero in a forward time simulation. The initial values for this simulation are the final values of the states just before the transition begins. The time interval for the second phase can be found by simulating the forward time system with the initial values for the simulation being the final values of the states when the current reaches zero. When the output voltage in this simulation reaches the required value denoted by v_{tb}, the elapsed time is the time interval for the second phase of the transition. The third phase time interval can be computed by finding the time required for the inductor current to reach zero in a reverse time simulation. The initial values for this simulation are taken from the desired operating point of the new load.

The parameters used in the previous simulations require a DCM transition process. Thus, different parameter values are used to demonstrate the CCM transition process. The parameters used to conduct the simulation to demonstrate the CCM transition process use the values shown in Table 4.6.

Table 4.6
Parameters for simulating a step decrease in load for a boost converter with a nonlinear saturating inductor (CCM)

Parameter	Value
V_s	200 V
R_L	1 $m\Omega$
$L_{nominal}$	20 mH
N	140
C	10 mF
$R_{load,1}$	8 Ω
$R_{load,2}$	32 Ω
$f_{sw,q1}$	10 kHz
$v_{c,ref}$	400 V

The step change in load is

$$R_{load} = \begin{cases} R_{load,1} & t < 0.001 \\ R_{load,2} & \text{otherwise} \end{cases} \tag{4.8}$$

where, R_{load} is the load connected to the converter, $R_{load,1}$ is the value of the load before the transition, and $R_{load,2}$ is the value of the load after the transition. The plots for the results of the simulation of the transition process can be seen in Figure 4.7 and Figure 4.8. Figure 4.7 shows the inductor current and Figure 4.8 shows the capacitor voltage. Figure 4.7 shows the two phases of the transition process, and it also shows that the converter with these parameters is barely in CCM. Important performance metrics logged in the simulation are given in Table 4.7.

Parameter values used in the previous chapter can be used to conduct a simulation

Table 4.7
Performance metrics from the simulation of a step decrease in load for a boost converter with a nonlinear saturating inductor (CCM)

Performance metric	Value
Transition time	2754.56 μs
Minimum i_L	2.86558 A
Peak v_c	401.861 V
Energy loss during transition	1.57203 mJ

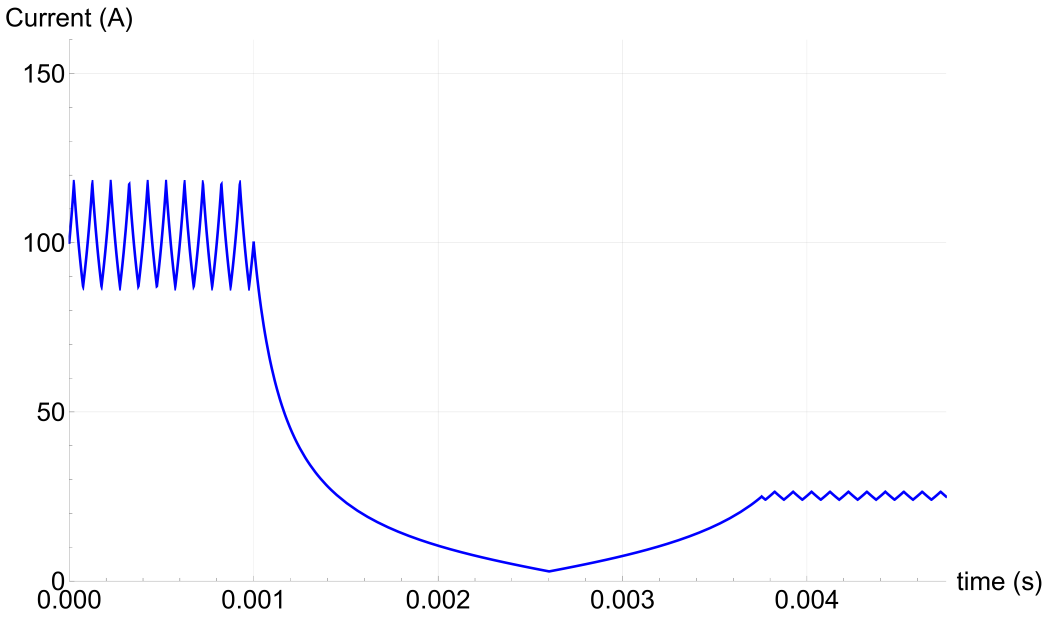

Figure 4.7: Inductor current in the boost converter with a nonlinear saturating inductor for a step decrease in load (CCM)

to demonstrate the DCM transition process. The parameters used to conduct the simulation to demonstrate the DCM transition process use the values shown in Table 4.8.

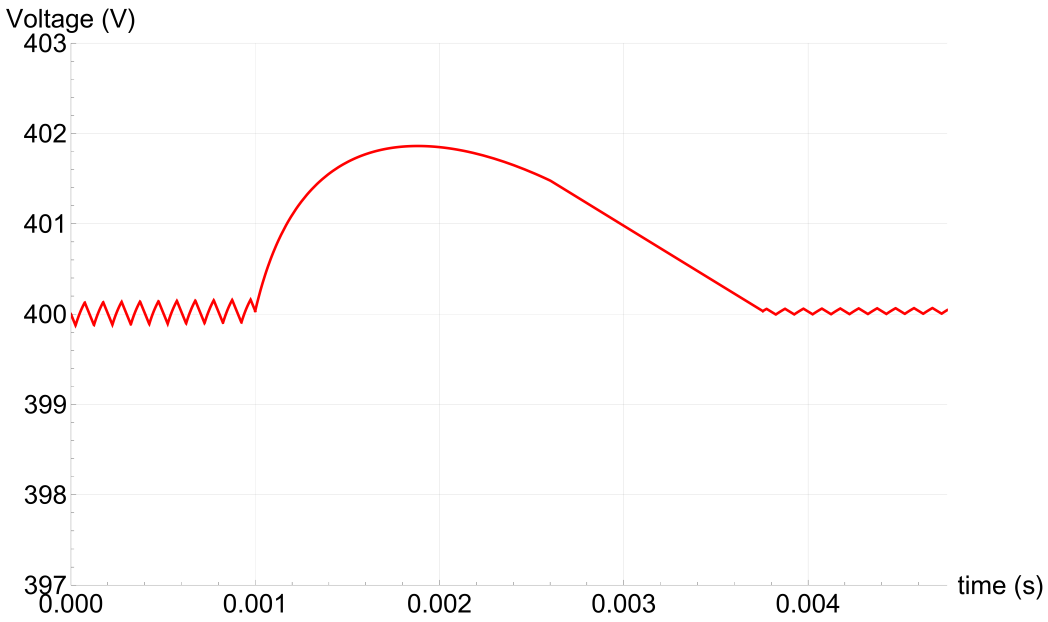

Figure 4.8: Capacitor voltage in the boost converter with a nonlinear saturating inductor for a step decrease in load (CCM)

Table 4.8
Parameters for simulating a step decrease in load for a boost converter with a nonlinear saturating inductor (DCM)

Parameter	Value
V_s	200 V
R_L	1 $m\Omega$
$L_{nominal}$	1 mH
N	32
C	1 mF
$R_{load,1}$	8 Ω
$R_{load,2}$	32 Ω
$f_{sw,q1}$	10 kHz
$v_{c,ref}$	400 V

The step change in load is

$$R_{load} = \begin{cases} R_{load,1} & t < 0.0005 \\ R_{load,2} & \text{otherwise} \end{cases} \tag{4.9}$$

where, R_{load} is the load connected to the converter, $R_{load,1}$ is the value of the load before the transition, and $R_{load,2}$ is the value of the load after the transition. The plots for the results of the simulation of the transition process can be seen in Figure 4.9 and Figure 4.10. Figure 4.9 shows the inductor current and Figure 4.10 shows the capacitor voltage. Figure 4.9 shows the three phases of the DCM transition process. Important performance metrics logged in the simulation are given in Table 4.9.

Table 4.9
Performance metrics from the simulation of a step decrease in load for a boost converter with a nonlinear saturating inductor (DCM)

Performance metric	Value
Transition time	932.889 μs
Minimum i_L	0 A
Peak v_c	408.302 V
Energy loss during transition	0.699988 mJ

4.3.2 Transition process for a CIBR boost converter

The transition is largely based on previous research that uses bang-bang control for minimizing transition time [17], and the switch state reversals shown above. The modifications from the CIBR topology augment the control law utilized previously. For a step decrease in the load for a CIBR boost converter, the control strategy helps the converter transition in two phases. Similar to the step increase in load transition, this is an open loop process, and all the required timings are pre-calculated. Unlike

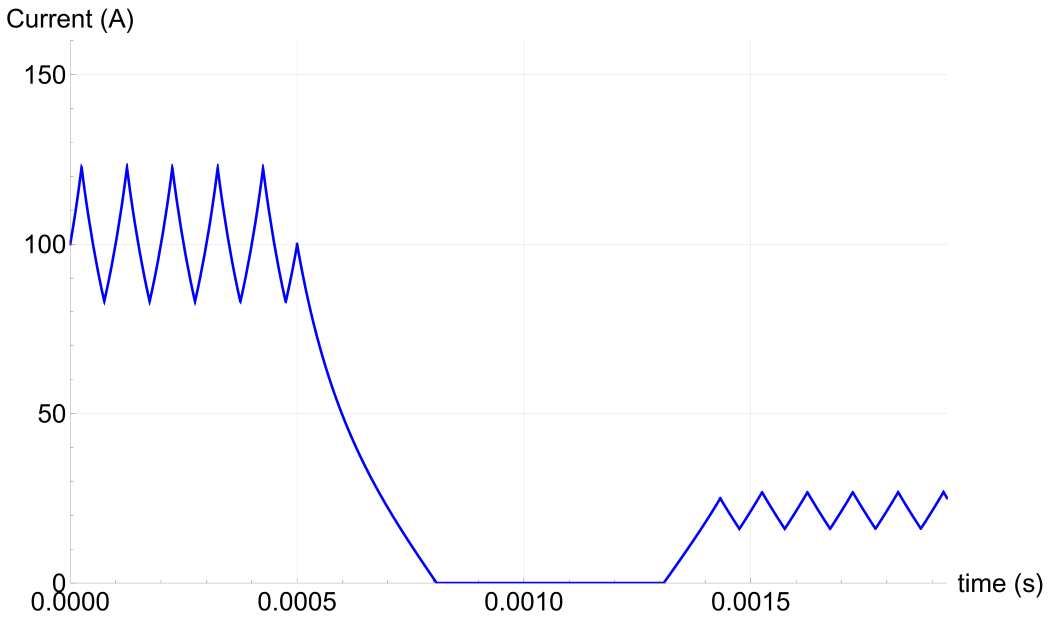

Figure 4.9: Inductor current in the boost converter with a nonlinear saturating inductor for a step decrease in load (DCM)

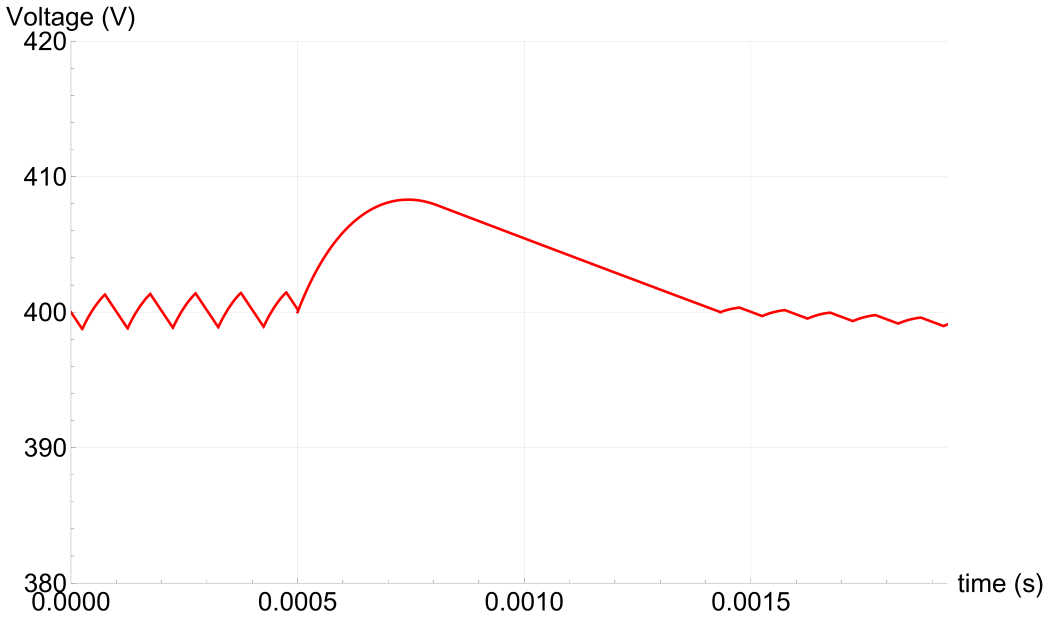

Figure 4.10: Capacitor voltage in the boost converter with a nonlinear saturating inductor for a step decrease in load (DCM)

the transition process for the step increase in load, here, the transition process begins at the moment of the transition of the load and marks the beginning of its first phase. When the current through the first coil is higher than the operating point of the corresponding load, it pushes the output voltage higher. Thus when the load switches to a lower level, the output voltage starts rising due to the initial value of the current being higher than the operating point for the lower load. Here, the bleed off resistor is switched ON to not just prevent the rise in output voltage, but also to force it below the desired steady state value. Thus, for the first phase of the transition process, the bleed off resistor is switched ON and 'q1' i.e. the first coil is switched OFF. After a certain time interval, the bleed off resistor is also switched OFF. This marks the end of the first phase and the beginning of the second phase of the transition process. At the beginning of the second phase of the transition, the current through the first coil is still higher than the required final value, but now the output voltage is lower than the required steady state value. During this phase, the bleed off resistor and 'q1' are OFF for a specific time interval. As the initial value of the current was higher than the required final value and the output voltage was lower, the current keeps falling towards the desired value which makes the output voltage rise. At the end of the second phase of the transition which is also the end of the full transition, the current falls to the required value and the output voltage rises to the required value. The converter now reverts back to duty cycle control. As with the previously seen transition processes, these time intervals are what make the process

work properly. The time intervals for the first and second phases of the transition can be found by minimizing the sum of the square errors for the current through the first coil and output voltage from the forward time trajectories of the system (where 'q1' is OFF and 'q3' is ON) and the reverse time trajectories of the system (where 'q1' and 'q3' are OFF).

$$\min J(t_f, t_r) = (v_c(t_f) - v_c(t_r))^2 + (i_1(t_f) - i_1(t_r))^2 \tag{4.10}$$

where, J is the cost function, t_f is the forward time, t_r is the reverse time, $v_c(t_f)$ and $i_1(t_f)$ represent the forward time trajectories, and $v_c(t_r)$ and $i_1(t_r)$ represent the reverse time trajectories. The initial values for the forward time trajectories are the final values seen just before the transition process begins, and the initial values for the reverse time trajectories are taken from the desired operating point of the system at the new load. The values for t_f and t_r that minimize the cost function are the required time intervals. Unlike the transition process for the step increase in load, weighting any of the trajectories is not necessary to get accurate results because both variables have a similar order of magnitude. An important factor to be noted for this transition process to work is that the bleed off resistor needs to have such a value that when aggregated with the new load, they need to be larger than the load the converter is transitioning from. As mentioned previously: "When the current through the first coil is higher than the operating point of the corresponding load, it pushes the output voltage higher." Thus, the reason the aggregated load needs to be higher than the

load the converter is transitioning from is that otherwise, the control strategy will not be able to force the current and the output voltage follow trajectories that make this transition process possible.

The parameters used to demonstrate the CCM transition process will be used to conduct a simulation to demonstrate the same transition using the new model and technique. These parameters are shown in Table 4.10.

Table 4.10
Parameters for simulating a step decrease in load for a CIBR boost converter (CCM-parameters)

Parameter	Value
V_s	200 V
R_{L_1}	1 $m\Omega$
R_{L_2}	1 $m\Omega$
$L_{1,nominal}$	20 mH
N_1	140
$L_{2,nominal}$	20 mH
N_2	140
R_{bo}	8 Ω
C	10 mF
$R_{load,1}$	8 Ω
$R_{load,2}$	32 Ω
$f_{sw,q1}$	10 kHz
$v_{c,ref}$	400 V

The step change in load is

$$R_{load} = \begin{cases} R_{load,1} & t < 0.0005 \\ R_{load,2} & \text{otherwise} \end{cases} \tag{4.11}$$

where, R_{load} is the load connected to the converter, $R_{load,1}$ is the value of the load before the transition, and $R_{load,2}$ is the value of the load after the transition. The plots for the results of the simulation of the transition process can be seen in Figure 4.11 and Figure 4.12. Figure 4.11 shows the inductor current and Figure 4.12 shows the capacitor voltage. Figure 4.12 shows the two phases of the transition process, and it also shows that the deviation in voltage during the transition is negligible and almost within the steady state ripple. Important performance metrics logged in the simulation are given in Table 4.11. As the current follows a direct trajectory between steady states and the voltage deviation is within the steady state ripple, the performance metrics of minimum i_1 and peak v_c are not applicable in Table 4.11.

Table 4.11
Performance metrics from the simulation of a step decrease in load for a CIBR boost converter (CCM-parameters)

Performance metric	Value
Transition time	462.251 μs
Minimum i_1	N/A
Peak v_c	N/A
Energy loss during transition	9246.83 mJ

The parameters used to demonstrate the DCM transition process will be used to conduct a simulation to demonstrate the same transition using the new model and technique. The parameters used to conduct this simulation use the values shown in Table 4.12.

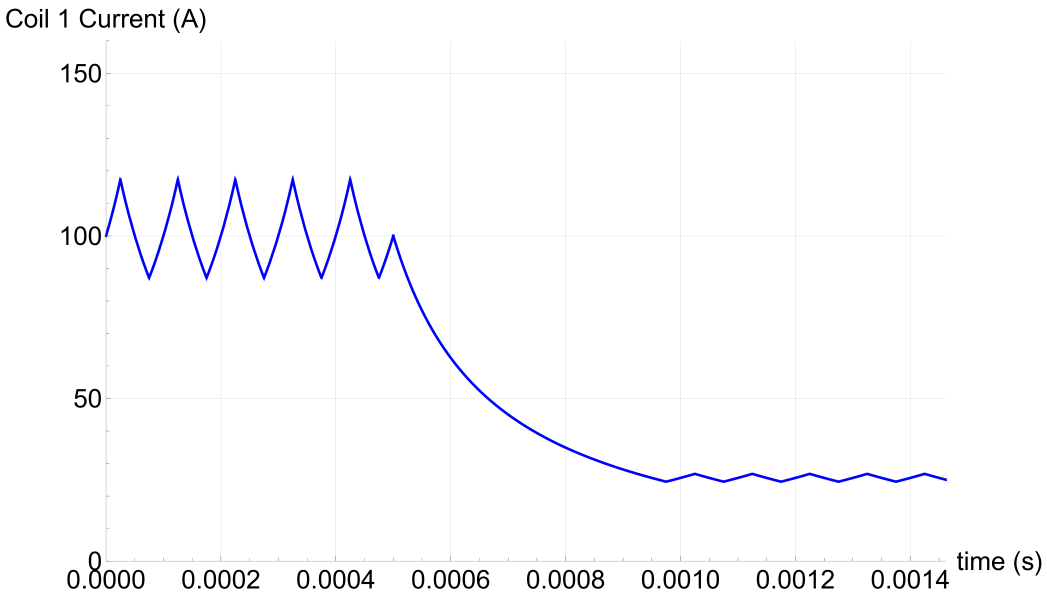

Figure 4.11: Coil 1 current in the CIBR boost converter for a step decrease in load (CCM-parameters)

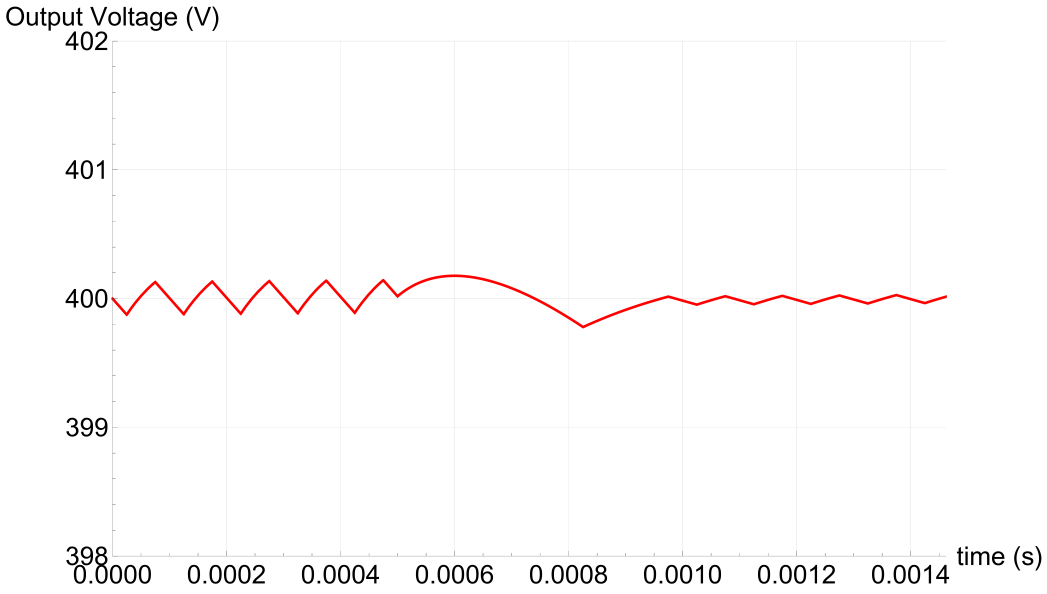

Figure 4.12: Capacitor voltage in the CIBR boost converter for a step decrease in load (CCM-parameters)

Table 4.12
Parameters for simulating a step decrease in load for a CIBR boost converter (DCM-parameters)

Parameter	Value
V_s	200 V
R_{L_1}	1 $m\Omega$
R_{L_2}	1 $m\Omega$
$L_{1,nominal}$	1 mH
N_1	32
$L_{2,nominal}$	1 mH
N_2	32
R_{bo}	8 Ω
C	1 mF
$R_{load,1}$	8 Ω
$R_{load,2}$	32 Ω
$f_{sw,q1}$	10 kHz
$v_{c,ref}$	400 V

The step change in load is

$$R_{load} = \begin{cases} R_{load,1} & t < 0.0005 \\ R_{load,2} & \text{otherwise} \end{cases} \tag{4.12}$$

where, R_{load} is the load connected to the converter, $R_{load,1}$ is the value of the load before the transition, and $R_{load,2}$ is the value of the load after the transition. The plots for the results of the simulation of the transition process can be seen in Figure 4.13 and Figure 4.14. Figure 4.13 shows the inductor current and Figure 4.14 shows the capacitor voltage. Figure 4.13 shows that the deviation in voltage during the transition is negligible and within the steady state ripple. The first phase of the transition can be seen due to hump in the voltage trajectory. The second phase is

lasts for a small time and its effect can be seen in the voltage trajectory where it climbs towards the steady state value just after the hump. Important performance metrics logged in the simulation are given in Table 4.13. As the current follows a direct trajectory between steady states and the voltage deviation is within the steady state ripple, the performance metrics of minimum i_1 and peak v_c are not applicable in Table 4.13.

Table 4.13
Performance metrics from the simulation of a step decrease in load for a CIBR boost converter (DCM-parameters)

Performance metric	Value
Transition time	191.739 μs
Minimum i_1	N/A
Peak v_c	N/A
Energy loss during transition	3848.29 mJ

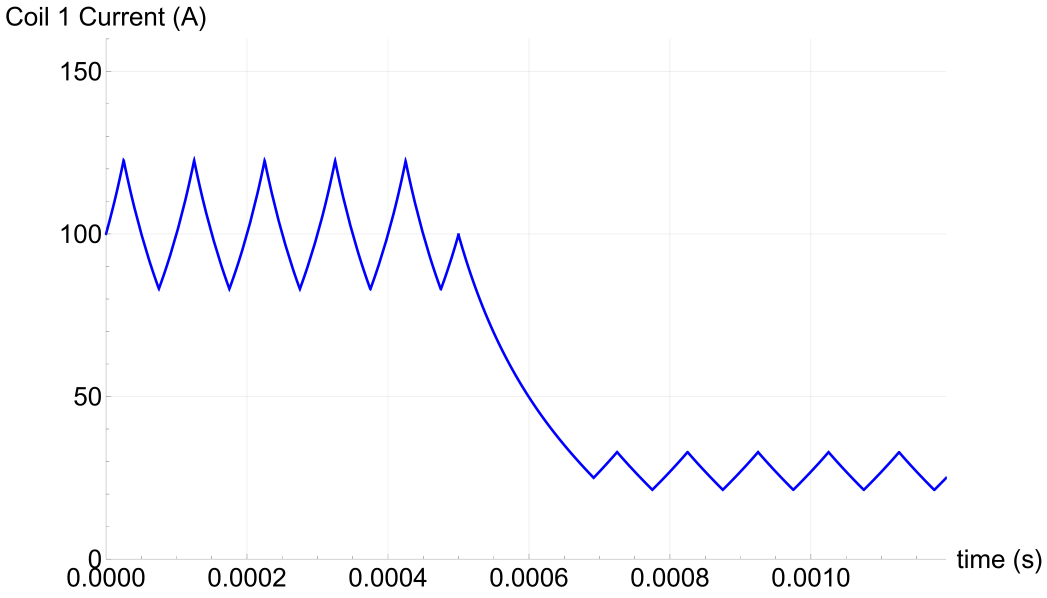

Figure 4.13: Coil 1 current in the CIBR boost converter for a step decrease in load (DCM-parameters)

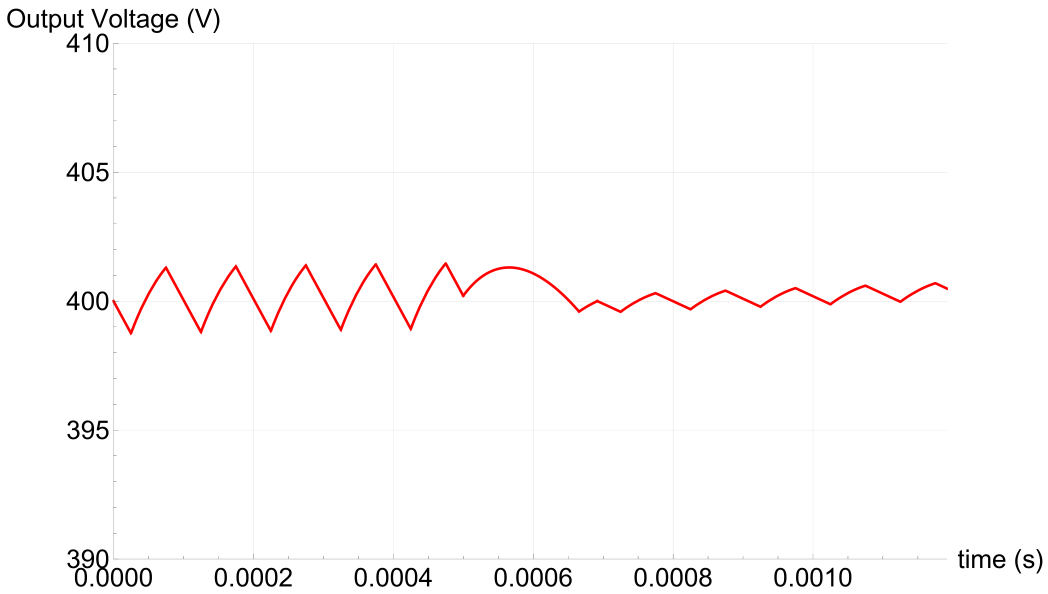

Figure 4.14: Capacitor voltage in the CIBR boost converter for a step decrease in load (DCM-parameters)

4.3.3 Comparison of the transition processes

Comparison of the CIBR boost converter and the boost converter with a nonlinear saturating inductor for a step decrease in load can be seen in Table 4.14 and Table 4.15. These comparisons are for the results obtained using the CCM parameters and DCM parameters respectively.

For both sets of parameters, the reduction in transition time is pretty high, which is a substantial improvement. The new technique also has the advantage of having a direct trajectory between steady states for the current without any deviations. Also, the deviations in the output voltage are so small that they are within the steady

Table 4.14
Comparison between boost converter with a nonlinear saturating inductor and CIBR boost converter (CCM-parameters)

Performance metric	Nonlin. sat. ind.	CIBR	Improvement
Transition time	2754.56 μs	462.251 μs	83.2153%
Minimum inductor current	2.86558 A	N/A	N/A
Peak voltage	401.861 V	N/A	N/A
Energy loss during transition	1.57203 mJ	9246.83 mJ	5882.095x worse

Table 4.15
Comparison between boost converter with a nonlinear saturating inductor and CIBR boost converter (DCM-parameters)

Performance metric	Nonlin. sat. ind.	CIBR	Improvement
Transition time	932.889 μs	191.739 μs	79.447%
Minimum inductor current	0 A	N/A	N/A
Peak voltage	408.302 V	N/A	N/A
Energy loss during transition	0.699988 mJ	3848.29 mJ	5497.65x worse

state ripple amplitudes. The results show a drawback for using the CIBR topology for both sets of parameters. As the transition time between steady states is reduced by bleeding off the excess energy, the significant amount of energy released through the bleed-off resistor makes the transition energy loss a few thousand times more than the loss seen with the old topology.

4.4 Stability of pulsed power loads

This section shows the stability maps for a boost converter with a linear inductor model and a CIBR boost converter when connected to a pulsed power load. The first

subsection demonstrates through simulations the behavior of a boost converter with a linear inductor model with duty cycle control when the system is stable and when it is unstable. The second subsection demonstrates through simulations the behavior of a CIBR boost converter with bang-bang control when the system is stable and when it is unstable. The third and final subsection compares the stability maps obtained using both topologies.

4.4.1 Stability map for a boost converter with a linear inductor

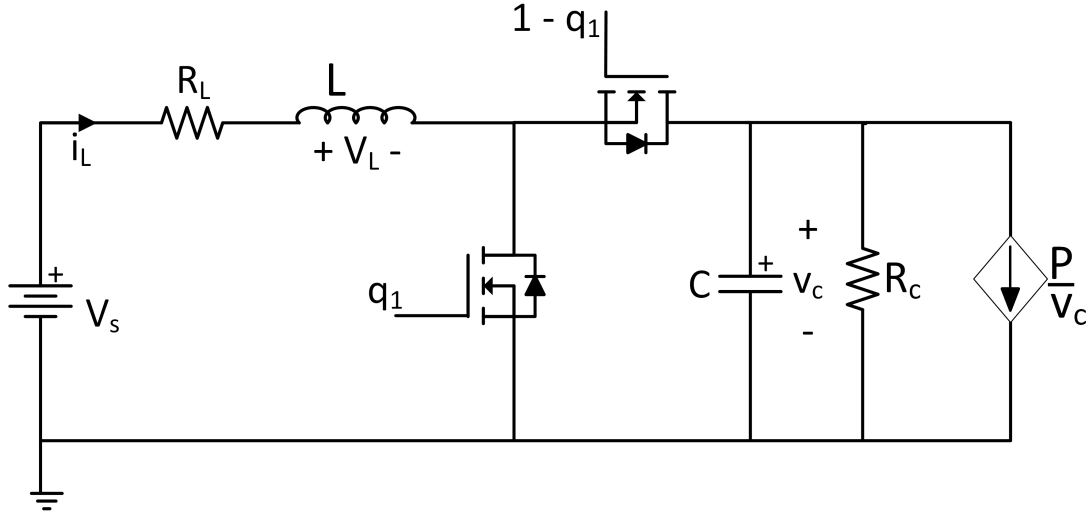

Figure 4.15: Boost converter with a linear inductor with a pulsed power load

In the previous research conducted to map the meta-stability margins for pulsed power loads, simulations used the average mode model of constant duty cycle control

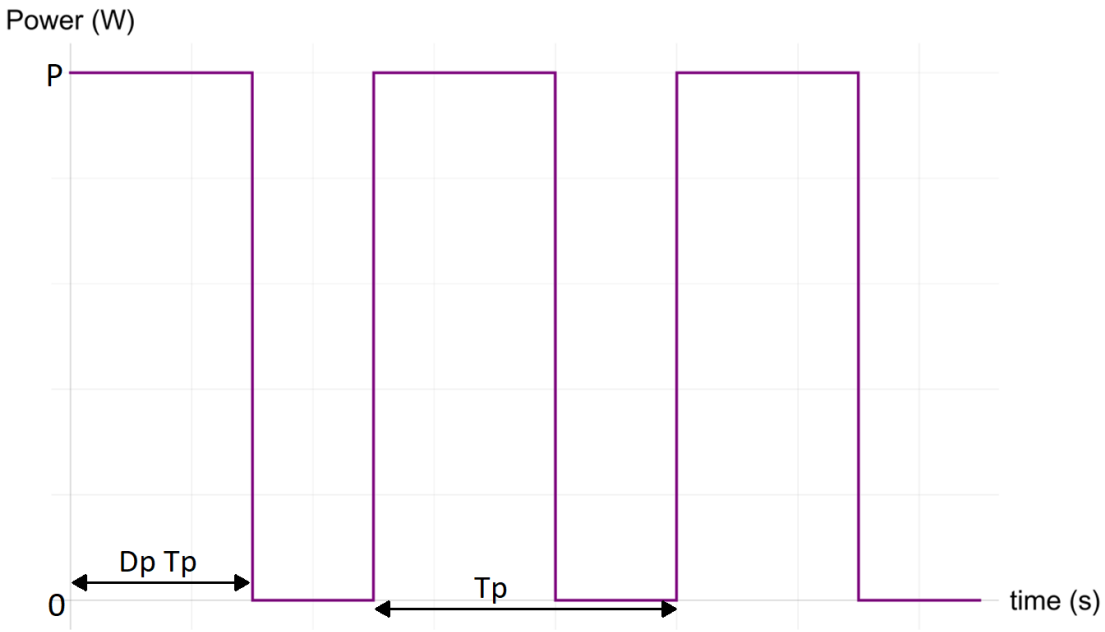

Figure 4.16: Pulsed power loads

for boost converters with a linear inductor model. The same will be done here. The model can be seen in Figure 4.15. The mathematical model remains largely the same from what was seen in Chapter 2, but the part of the equation for the load changes. Another difference is the use of the average mode model for switching. This slightly modified mathematical model is

$$L\frac{di_L}{dt} = V_s - i_L R_L - (1-d_1)v_c \tag{4.13}$$

$$C\frac{dv_c}{dt} = (1-d_1)i_L - \frac{v_c}{R_c} - \frac{P}{v_c} \tag{4.14}$$

where, R_c is the stabilizing resistor, d_1 is the duty cycle of the switch 'q1', and P denotes the pulsed power. In Figure 4.16, P is the power level, Tp is the time period of the pulse and Dp is the duty cycle of the pulse. The parameter values used for

conducting the simulations to demonstrate the system's behavior and to map the stability margins are listed in Table 4.16.

Table 4.16
Parameters for simulating a boost converter with a linear inductor with a pulsed power load

Parameter	Value
V_s	200 V
R_L	1 $m\Omega$
L	1 mH
C	1 mF
R_c	50 Ω
$v_{c,ref}$	400 V Ω
d_1	0.5

For certain nonlinear Single-Input-Single-Output (SISO) systems, describing functions can be used in conjunction with Nyquist analysis to assess the stability of limit cycles [43]. This method can be adapted to be applicable for multiple input systems [44]. In this thesis, stability is determined from the behavior of the system's states. The boost converter with a linear inductor model behaves in specific ways with constant duty cycle control when the system is stable and unstable. When the system is stable, the inductor current and output voltage have consistent bounded oscillations. This behavior can be seen in Figure 4.17 and Figure 4.18. When the system is unstable, the oscillations in the inductor current keep growing without bounds with each power pulse and the output voltage collapses to zero after a rapid growth in the amplitude of its oscillations. This behavior can be seen in Figure 4.19 and Figure 4.20. These simulations demonstrating stable and unstable behavior have the pulse power

level set at 6kW and the pulse power time period set at 0.2s. Figure 4.29 shows that for these parameter values, the pulse power duty cycle of 0.2 is stable and the pulse power duty cycle of 0.6 is unstable. From this behavior, it can be concluded that whether the system is unstable can be determined by surveilling the output voltage. Thus, the system can be classified as unstable by detecting a steady increase in the maximum amplitude of its oscillation for five power pulses or by detecting the output voltage collapsing to zero, whichever comes first. If this criterion is not satisfied, the system is classified as stable.

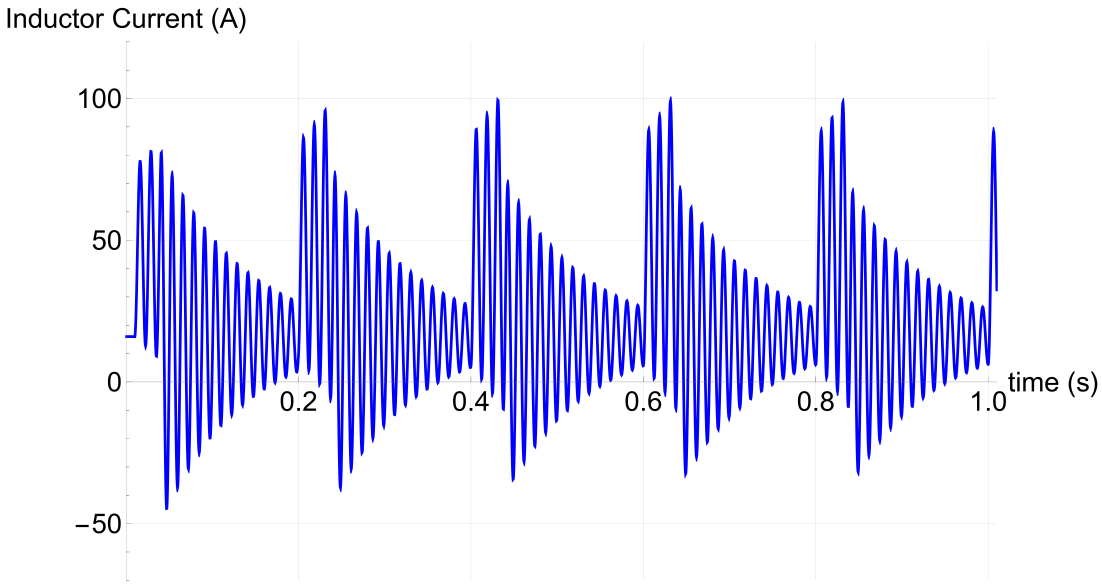

Figure 4.17: Inductor current for boost converter with a linear inductor with a pulsed power load when system is stable ($P = 6kW, Tp = 0.2s, Dp = 0.2$)

The stability margins are mapped by detecting the maximum duty cycle of the pulsed power for which the system is stable over a range of power levels and time periods for the pulsed power load. The stability map for the boost converter with a linear

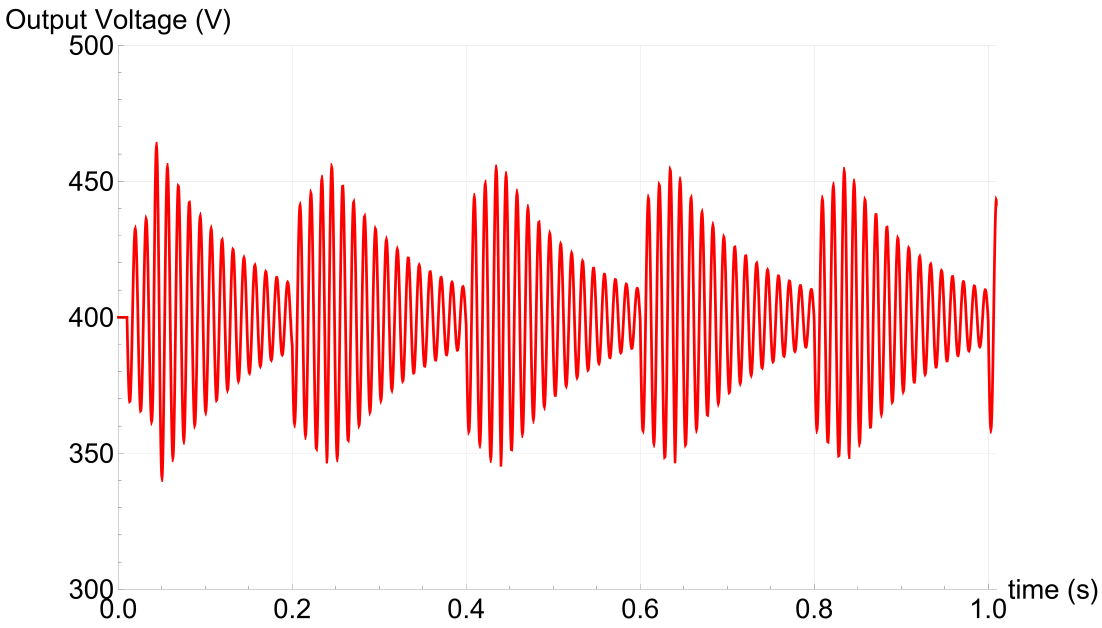

Figure 4.18: Output voltage for boost converter with a linear inductor with a pulsed power load when system is stable ($P = 6kW, Tp = 0.2s, Dp = 0.2$)

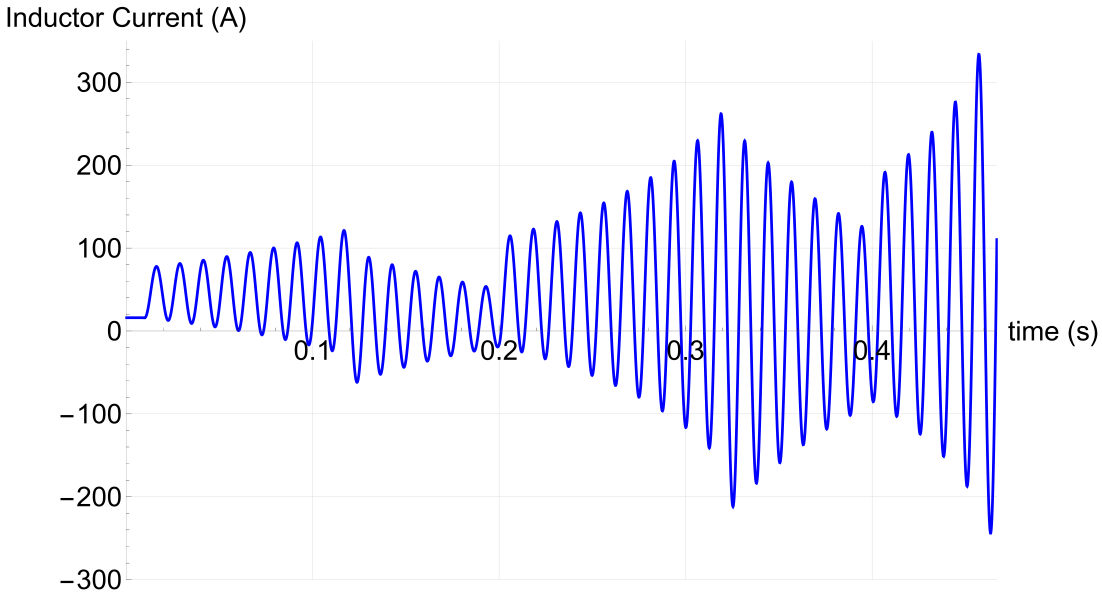

Figure 4.19: Inductor current for boost converter with a linear inductor with a pulsed power load when system is unstable ($P = 6kW, Tp = 0.2s, Dp = 0.6$)

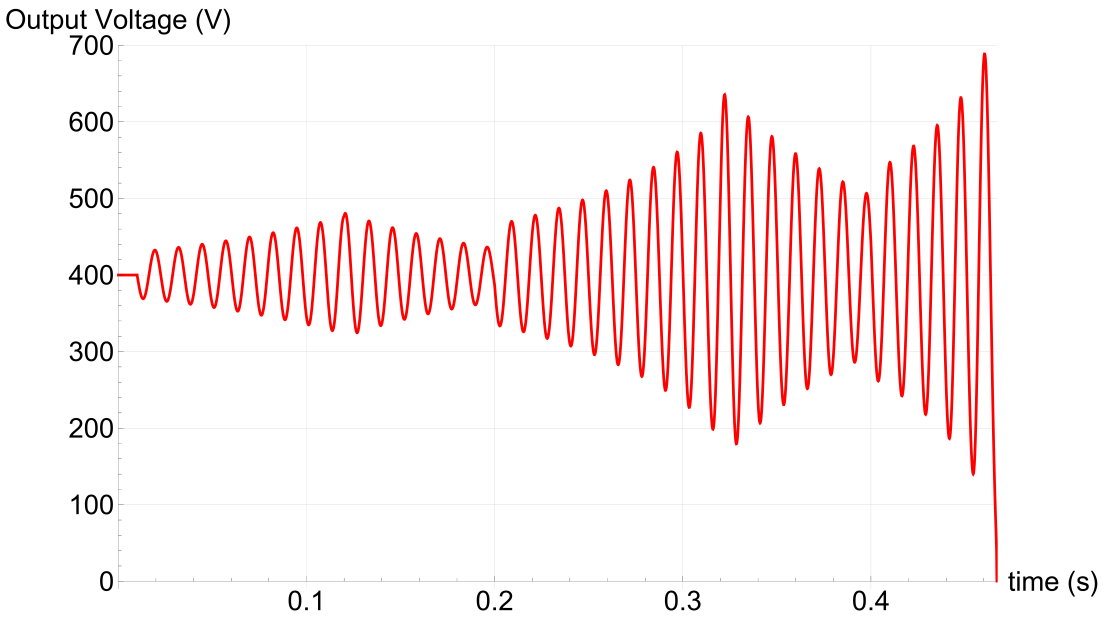

Figure 4.20: Output voltage for boost converter with a linear inductor with a pulsed power load when system is unstable ($P = 6kW, Tp = 0.2s, Dp = 0.6$)

inductor model and constant duty cycle control can be seen in Figure 4.21. The stability margins trend down as power level increases for a certain time period. Also, there are fluctuations in the margins with respect to the time period for a constant power level.

4.4.2 Stability map for a CIBR boost converter

To verify whether the CIBR boost converter leads to improvement in the meta-stability margins, the CIBR topology is simulated with pulsed power loads. To this end, the transition time intervals for each of the power levels to be simulated need to

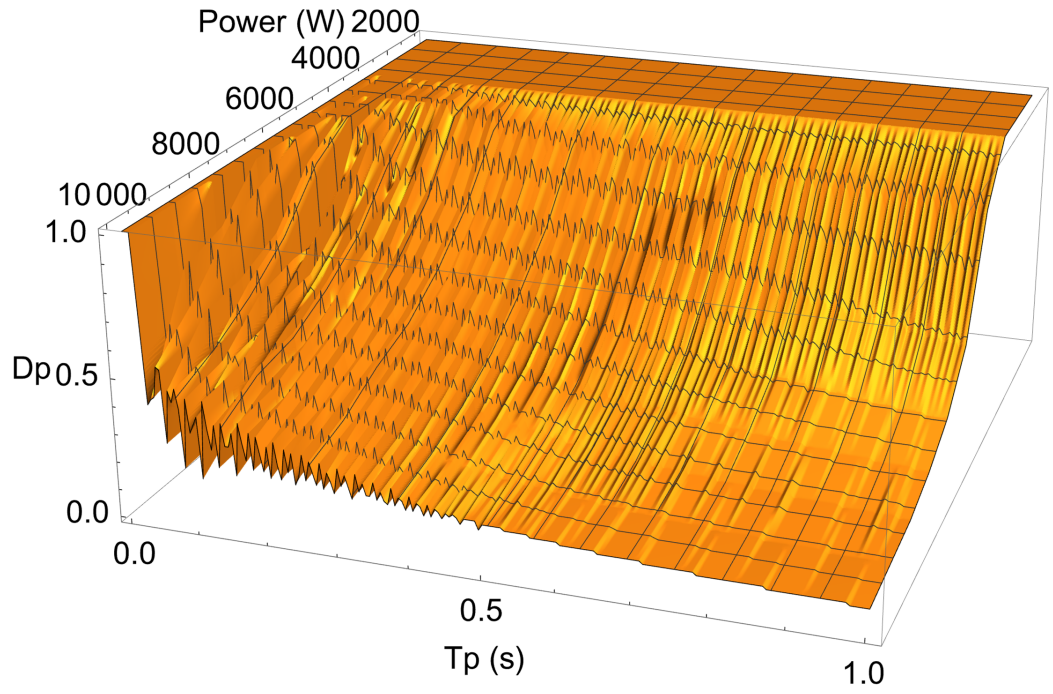

Figure 4.21: Stability map for boost converter with a linear inductor with a pulsed power load

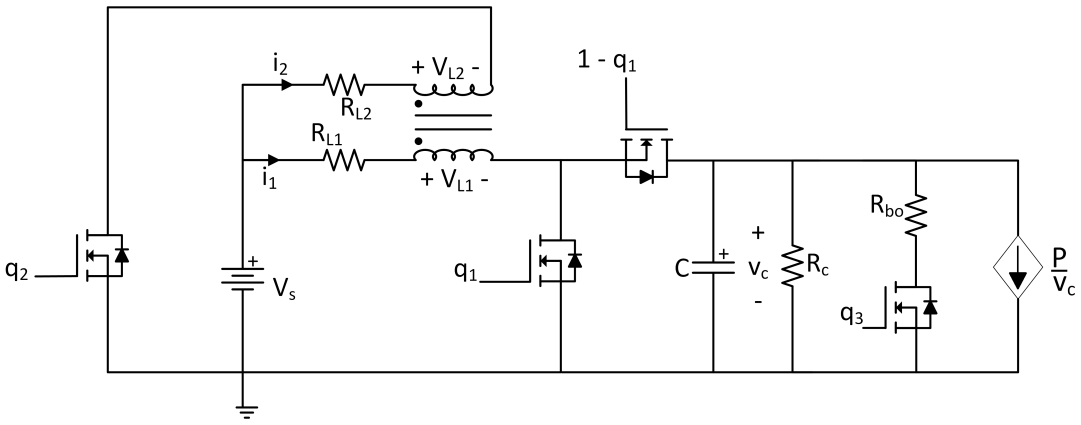

Figure 4.22: CIBR boost converter with a pulsed power load

be calculated. These include the time intervals for step-up and step-down changes to and from those power levels, respectively. The timings are stored in a look up table for easy access during the simulation. The model for this scenario can be seen in

Figure 4.22. The mathematical model remains largely the same from what was seen in Chapter 3, but the part of the equation for the load changes. Here too the average mode model is used for representing the switching of 'q1'. When 'q2' is ON

$$V_{L_1} = V_s - i_1 R_{L_1} - (1 - d_1) v_c \tag{4.15}$$

$$i_2 = q_2 \left(\frac{V_s - V_{L_2}}{R_{L_2}} \right) \tag{4.16}$$

$$C \, \frac{dv_c}{dt} = (1 - d_1) i_1 - q_3 \left(\frac{v_c}{R_{bo}} \right) - \frac{v_c}{R_c} - \frac{P}{v_c} \tag{4.17}$$

$$\frac{\lambda_{11}}{N_1} + \frac{\lambda_{22}}{N_2} = A_c \, a \, \arctan \left(b \, \left(\frac{N_1 \, i_1}{l_c} + \frac{N_2 \, i_2}{l_c} \right) \right) \tag{4.18}$$

$$\frac{\lambda_{11}}{N_1} - \frac{\lambda_{22}}{N_2} = A_c \, a \, \arctan \left(b \, \left(\frac{N_1 \, i_1}{l_c} - \frac{N_2 \, i_2}{l_c} \right) \right) \tag{4.19}$$

$$\frac{d\lambda_{11}}{dt} = \frac{N_2 \, V_{L_1} - k \, N_1 \, V_{L_2}}{(1 - k^2) N_2} \tag{4.20}$$

$$\frac{d\lambda_{22}}{dt} = \frac{N_1 \, V_{L_2} - k \, N_2 \, V_{L_1}}{(1 - k^2) N_1}. \tag{4.21}$$

When 'q2' is OFF

$$\frac{d\lambda_1}{dt} = V_s - i_1 R_{L_1} - (1 - d_1) v_c \tag{4.22}$$

$$C \, \frac{dv_c}{dt} = (1 - d_1) i_1 - q_3 \left(\frac{v_c}{R_{bo}} \right) - \frac{v_c}{R_c} - \frac{P}{v_c} \tag{4.23}$$

$$\frac{\lambda_1}{N_1} = A_c \, a \, \arctan \left(b \, \frac{N_1 \, i_1}{l_c} \right). \tag{4.24}$$

For pulsed power loads, the current jump phenomenon behaves the same with the same equation to quantify the jump. No changes are required in the current jump

model. The value of the current in the first coil after the jump is

$$i_1 = \frac{l_c}{b\,N_1}\,\tan\left(\frac{1}{A_c\,a}\,\left(\frac{\lambda_{11}}{N_1}+\frac{\lambda_{22}}{N_2}\right)\right). \tag{4.25}$$

For equations (4.15) through (4.25), R_c is the stabilizing resistor, d_1 is the duty cycle of the 'q1' switch, and P denotes the pulsed power. The parameter values used for conducting the simulations to demonstrate the system's behavior and to map the stability margins are listed in Table 4.17.

Table 4.17
Parameters for simulating a CIBR boost converter with a pulsed power load

Parameter	Value
V_s	200 V
R_{L_1}	1 $m\Omega$
R_{L_2}	1 $m\Omega$
$L_{1,nominal}$	1 mH
N_1	32
$L_{2,nominal}$	1 mH
N_2	32
C	1 mF
R_{bo}	16 Ω
R_c	50 Ω
$v_{c,ref}$	400 V Ω

The CIBR boost converter in conjunction with bang-bang control behaves in certain ways when the system is stable and unstable. When the system is stable, the inductor current and output voltage have bounded oscillations and may have fluctuations in the maximum amplitude for each power pulse for some sets of parameters. This

behavior can be seen in Figure 4.23 and Figure 4.24. When the system is unstable, the oscillations in the inductor current keep growing without bounds with each power pulse and so do the oscillations in the output voltage. This behavior can be seen in Figure 4.25 and Figure 4.26. These simulations demonstrating stable and unstable behavior have the pulse power level set at 6kW and the pulse power time period set at 0.2s. Figure 4.29 shows that for these parameter values, the pulse power duty cycle of 0.6 is stable and the pulse power duty cycle of 0.8 is unstable. From this behavior, it can be concluded that whether the system is unstable can be determined by surveilling the output voltage. Thus, the system can be classified as unstable by detecting a steady increase in the maximum amplitude of its oscillation for five power pulses. If this criterion is not satisfied, the system is classified as stable.

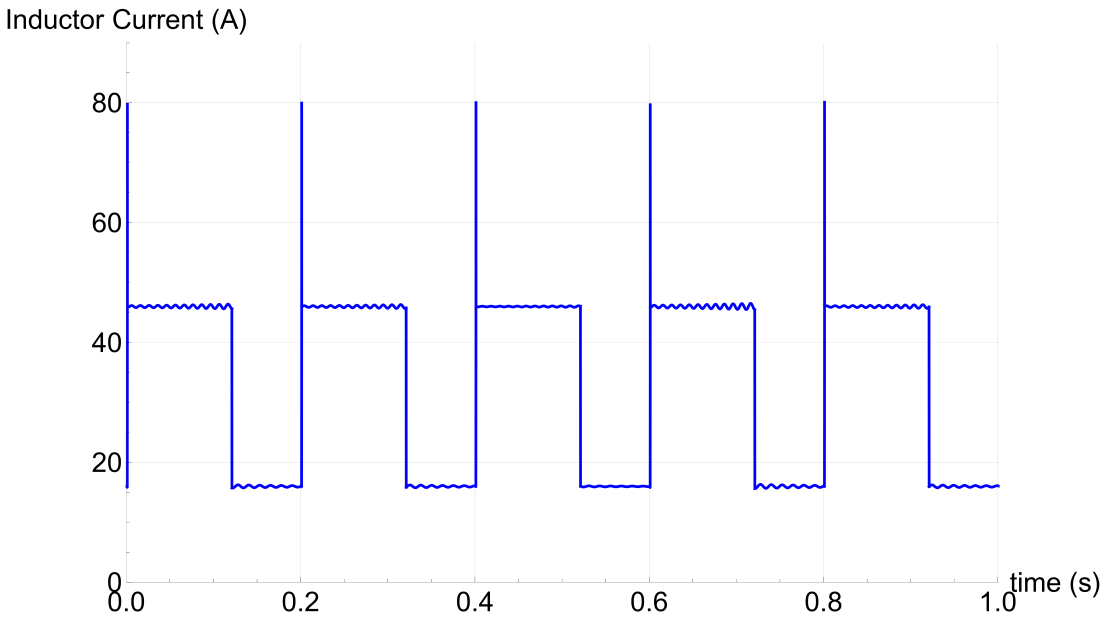

Figure 4.23: Inductor current for CIBR boost converter with a pulsed power load when system is stable ($P = 6kW, Tp = 0.2s, Dp = 0.6$)

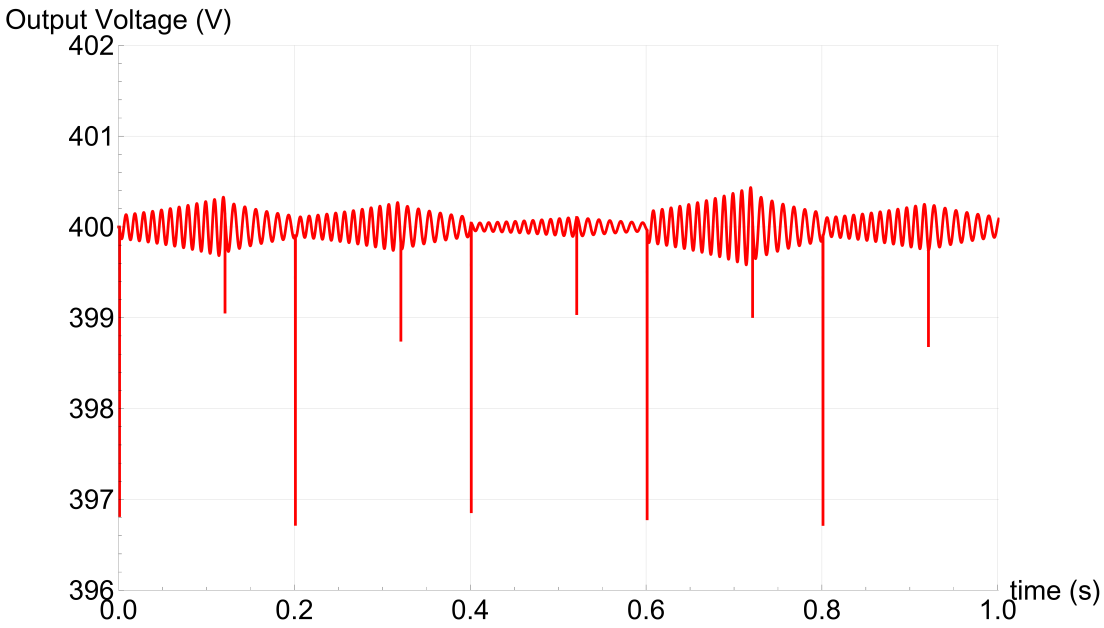

Figure 4.24: Output voltage for CIBR boost converter with a pulsed power load when system is stable ($P = 6kW, Tp = 0.2s, Dp = 0.6$)

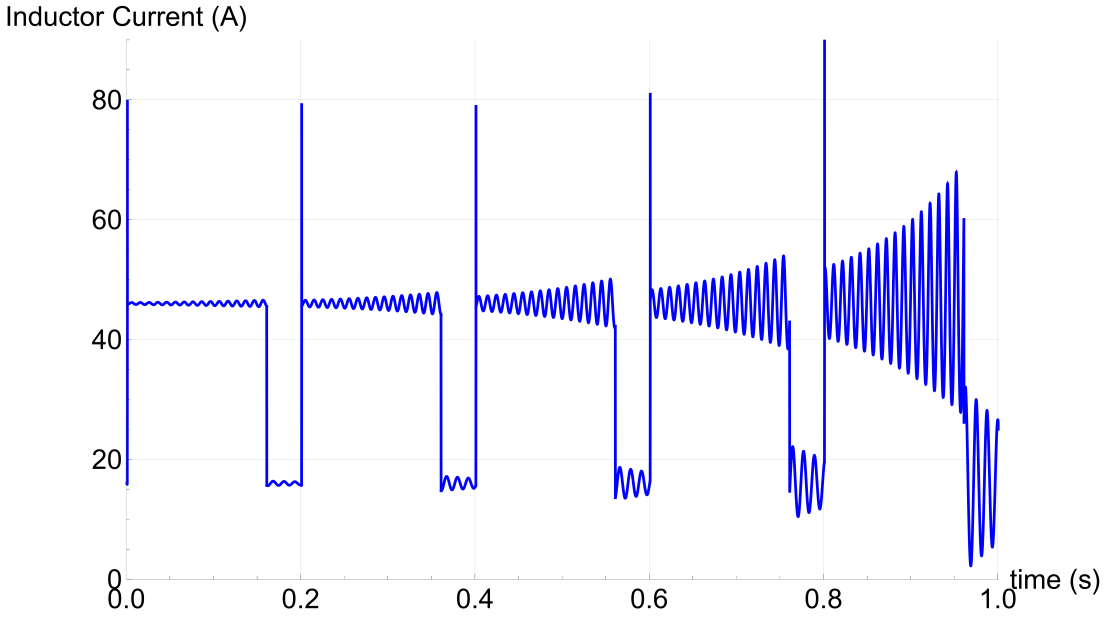

Figure 4.25: Inductor current for CIBR boost converter with a pulsed power load when system is unstable ($P = 6kW, Tp = 0.2s, Dp = 0.8$)

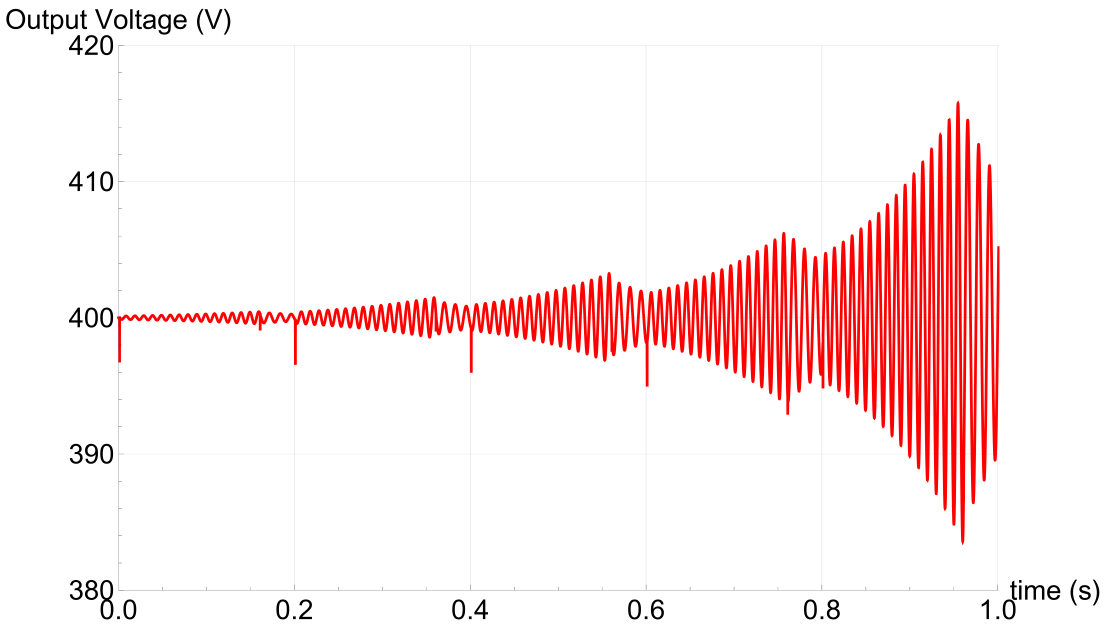

Figure 4.26: Output voltage for CIBR boost converter with a pulsed power load when system is unstable ($P = 6kW, Tp = 0.2s, Dp = 0.8$)

Similar to the process of mapping the stability margins seen previously, the margins are mapped by detecting the maximum duty cycle of the pulsed power for which the system is stable over a range of power levels and time periods for the pulsed power load. The stability map for the CIBR boost converter and bang-bang control can be seen in Figure 4.27. Even though the results are quantitatively different when compared to the previous map, qualitatively they are very similar. The stability margins trend down as power level increases for a certain time period, and there are fluctuations in the margins with respect to the time period for a constant power level.

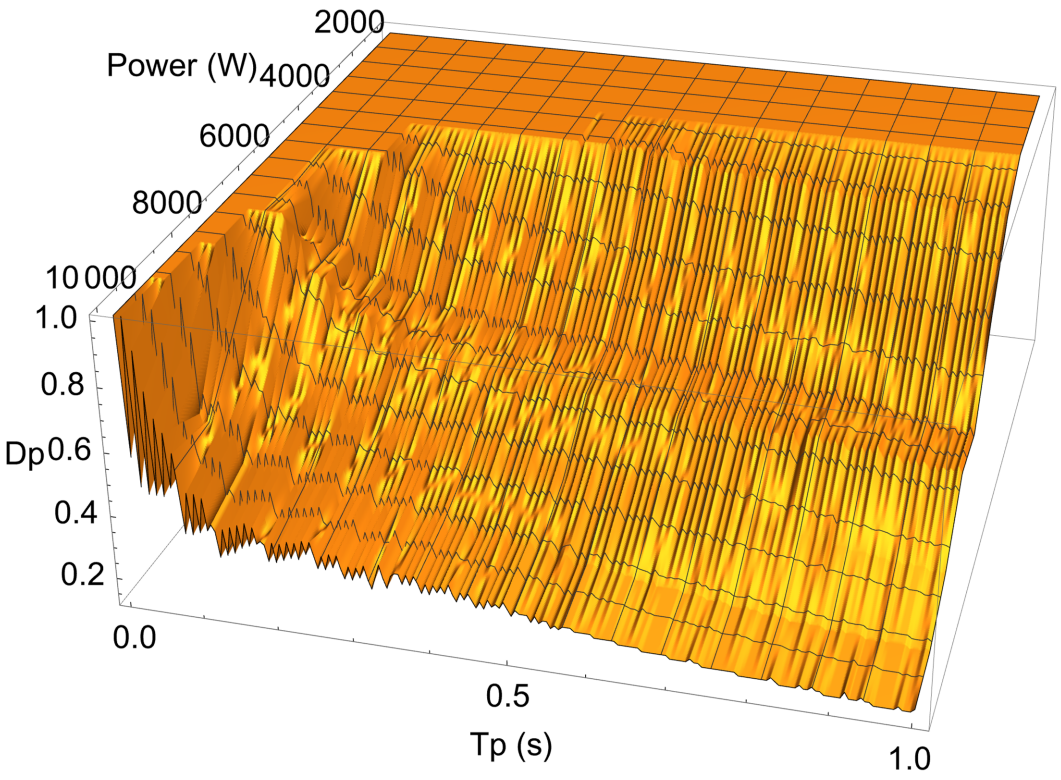

Figure 4.27: Stability map for CIBR boost converter with a pulsed power load

4.4.3 Comparison of the stability maps

The plot for the comparison of the stability maps for the linear inductor boost converter and the CIBR boost converter can be seen in Figure 4.28. A slice of this comparison plot at 6kW can be seen in Figure 4.29. A plot that shows the ripples in the stability margins in more detail can be seen in Figure 4.30. Figures 4.29 and 4.30 show that the boundary of the stability margin has ripples that could determine the operational regions for a system. If a certain load has a constant power level and

constant pulse duty cycle with varying time periods, the system may not be stable at all operating points. The system parameters determine when and how the system reacts to the load and changes in the load, and the load parameters determine when and how the load switches. Thus, if any system parameter is changed, a change is expected in the stability margin and the ripple seen in the stability margin. The stability margins and the ripples in the boundaries of the stability margins are different for three different nominal inductance values for a CIBR boost converter connected to a pulsed power load whose power level is at 5kW. Figure 4.31 shows that the stability margins and the ripples seen in the stability margins change when any system parameter is changed. As the nominal inductance increases, the width of the ripple increases and the average stability decreases. Thus, it can be confidently said that the ripple in the stability margin boundary must be a result of the system parameters and the parameters of the pulsed power, although a quantifiable relationship is hard to derive due to the numerical nature of the simulations.

Two thousand data points can be extracted if the stability margins are inspected at $1kW$ intervals for P and $0.005s$ intervals for Tp. For this sample size of two thousand data points, the average increase in the stability margins due to the CIBR topology and bang-bang control is 38.3317%. This is a substantial average improvement in the stability margins. Given in the subsequent chapter are conclusions from the results and comparisons seen in this chapter. It also discusses some avenues to carry this research forward.

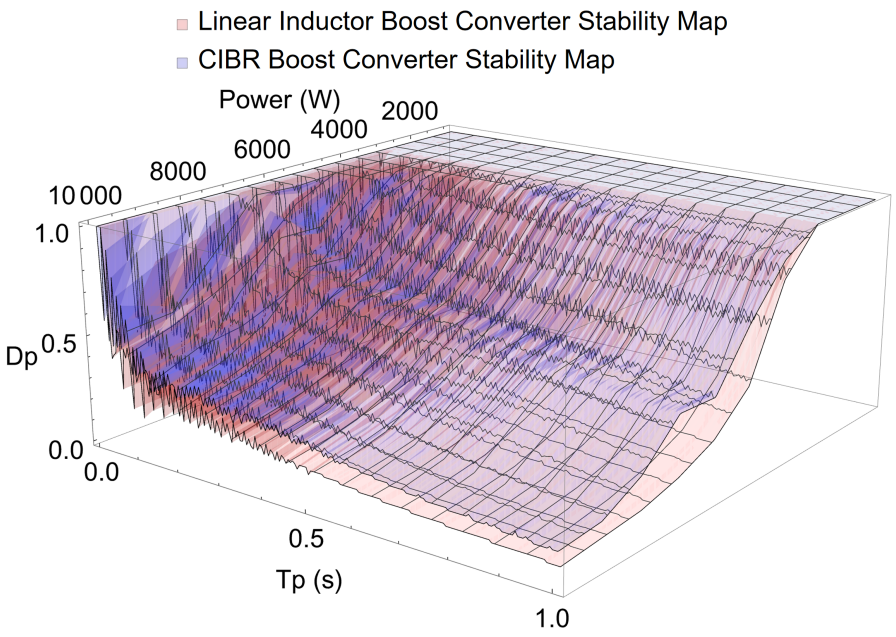

Figure 4.28: Comparison of the stability maps

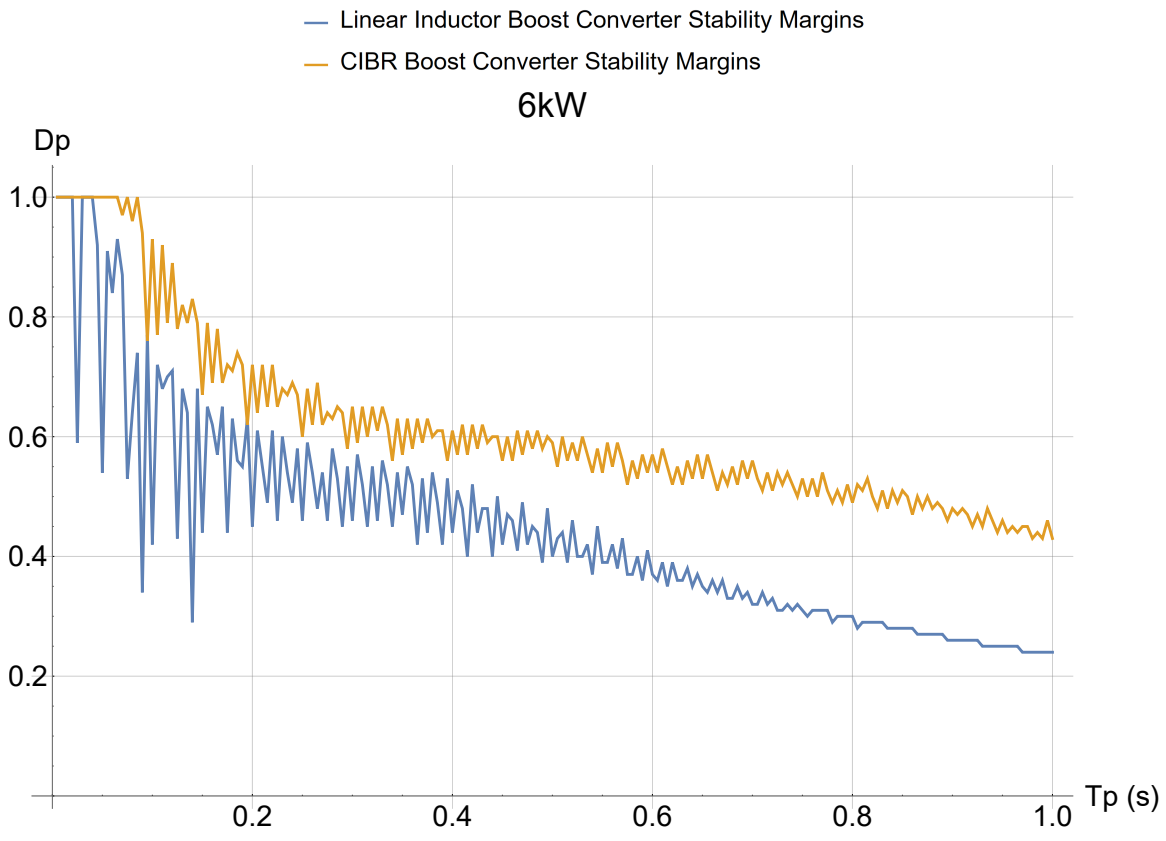

Figure 4.29: A slice of Figure 4.28 at 6kW

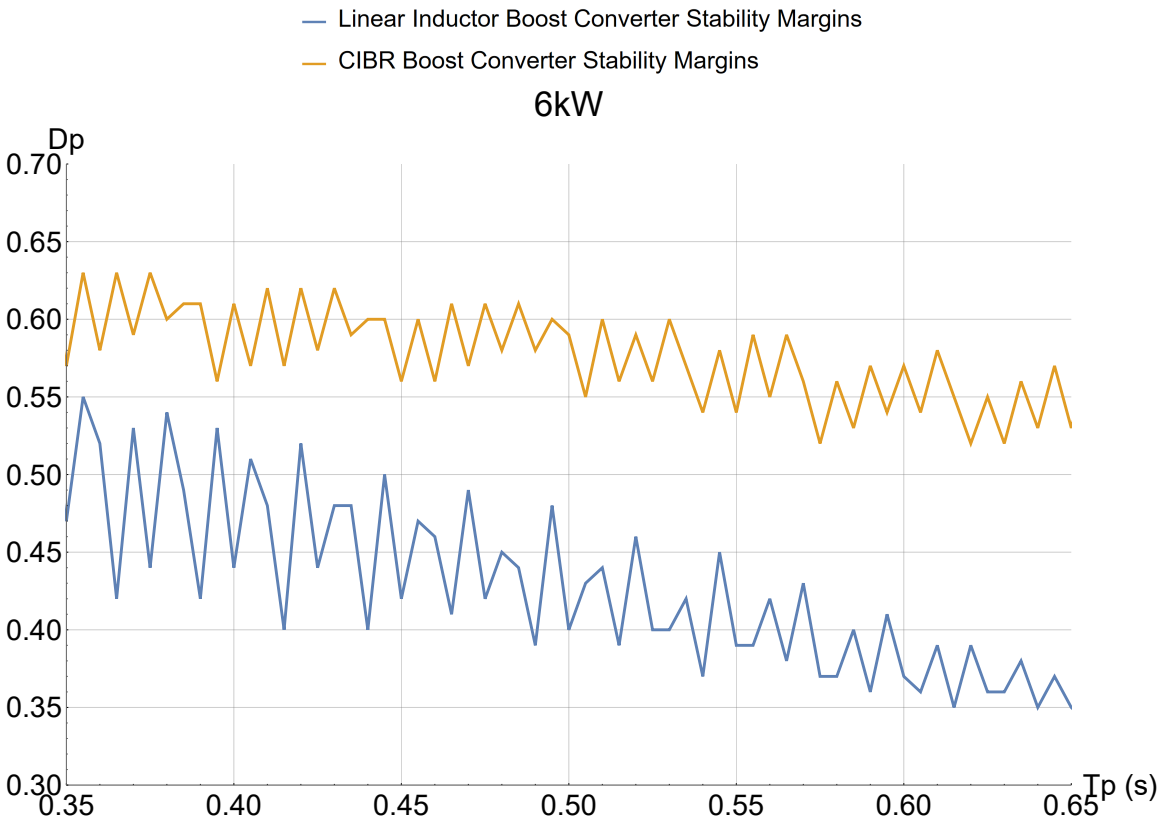

Figure 4.30: Zoomed in version of Figure 4.29

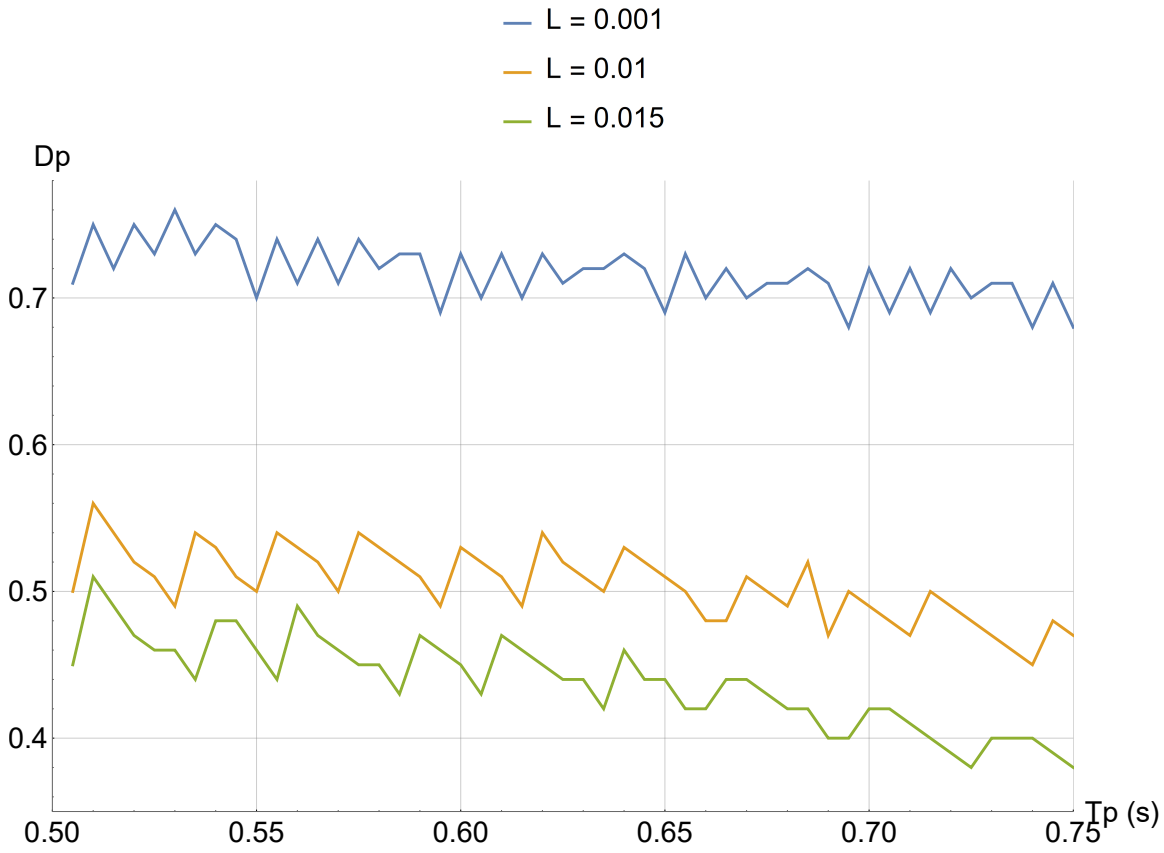

Figure 4.31: Stability margins for different nominal inductances for a CIBR boost converter with a pulsed power load ($P = 5kW$)

Chapter 5

Conclusion and future work

5.1 Conclusion

The results from the previous chapter show that the two main objectives of this thesis have been achieved. The primary objective of improving the dynamic characteristics has been achieved, which can be verified from the comparison tables for the old and new topologies. The second objective of improving the stability margins for pulsed power loads has been achieved, which can be verified from the last section of the previous chapter. The questions posed in the first chapter have also been adequately answered through the results. The questions about saturating the inductor core faster and modifying the topology to improve behavior for step changes in load

have been answered by the development of the CIBR topology. The CIBR boost converter topology is the product of the proposed solution. For step increases in load, it has been shown to improve dynamic characteristics for all performance metrics under consideration. For step decreases in load, the CIBR topology improves upon the old topology in all performance metrics except the energy lost during transition parameter. There is a massive increase in transition energy losses for step decreases in the load, because of the energy being bled-off through the bleed-off resistor. The application of the CIBR topology and bang-bang control for pulsed power loads has been shown to increase the meta-stability margins when compared to the previously used techniques by an average of 38.3317%. All these results have been in-line with the expectations.

5.2 Future work

The work done in this thesis leads to a few questions and ideas that can be researched in the future. The obvious next step is to validate the simulation results using Hardware-in-the-Loop (HiL) testing. This can be followed by building a prototype and collecting real world data from it. Research can also be done to improve the accuracy of the mathematical model used to simulate different scenarios. The coupled inductor was modeled assuming no flux leakage and no hysteresis. In the future, flux leakage and hysteresis can be added into the inductor core's magnetic

model to improve the accuracy of the coupled inductor model. For step increases in load, the current jump phenomenon assumes lossless transfer of energy. Here too, the accuracy of the mathematical model can be increased by factoring in a parameter for the efficiency of the energy transfer. Also, system parameters can be changed to see what effect they have on the performance of the CIBR boost converter. In this thesis, the CIBR topology is used with bang-bang control to improve dynamic characteristics. These modifications made to a typical boost converter's topology to create the CIBR topology can be used for purposes other than improving the dynamic characteristics. An idea that comes to mind is applying Sliding Mode Control (SMC) to the bleed-off resistor to prevent over voltage during operation. Another research area that can be worked on is to find a quantifiable relationship between the system and load parameters and the stability margins for pulsed power loads seen in the previous chapter.

References

[1] A. Lachichi, "Dc/dc converters for high power application: A survey," in *2013 3rd International Conference on Electric Power and Energy Conversion Systems*, pp. 1–4, 2013.

[2] C. Shi, B. Miller, K. Mayaram, and T. Fiez, "A multiple-input boost converter for low-power energy harvesting," *IEEE Transactions on Circuits and Systems II: Express Briefs*, vol. 58, no. 12, pp. 827–831, 2011.

[3] A. Stratakos, S. Sanders, and R. Brodersen, "A low-voltage cmos dc-dc converter for a portable battery-operated system," in *Proceedings of 1994 Power Electronics Specialist Conference - PESC'94*, vol. 1, pp. 619–626 vol.1, 1994.

[4] R. de Castro, J. P. Trovão, P. Pacheco, P. Melo, P. G. Pereirinha, and R. E. Araújo, "Dc link control for multiple energy sources in electric vehicles," in *2011 IEEE Vehicle Power and Propulsion Conference*, pp. 1–6, 2011.

[5] O. Hegazy, J. Van Mierlo, and P. Lataire, "Modeling and control of interleaved

multiple-input power converter for fuel cell hybrid electric vehicles," in *International Aegean Conference on Electrical Machines and Power Electronics and Electromotion, Joint Conference*, pp. 408–414, 2011.

[6] "Circuit protection in microcontrollers: Brownout detection." `https://www.arrow.com/en/research-and-events/articles/circuit-protection-in-microcontrollers`. Accessed: 2020-03-28.

[7] W. W. Weaver, R. D. Robinett, D. G. Wilson, and R. C. Matthews, "Metastability of pulse power loads using the hamiltonian surface shaping method," *IEEE Transactions on Energy Conversion*, vol. 32, no. 2, pp. 820–828, 2017.

[8] L. N. Domaschk, A. Ouroua, R. E. Hebner, O. E. Bowlin, and W. B. Colson, "Coordination of large pulsed loads on future electric ships," *IEEE Transactions on Magnetics*, vol. 43, no. 1, pp. 450–455, 2007.

[9] Z. Dong, X. Cong, Z. Xiao, X. Zheng, and N. Tai, "A study of hybrid energy storage system to suppress power fluctuations of pulse load in shipboard power system," in *2020 International Conference on Smart Grids and Energy Systems (SGES)*, pp. 437–441, 2020.

[10] H. Smolleck, S. Ranade, N. Prasad, and R. Velasco, "Effects of pulsed-power loads upon an electric power grid," *IEEE Transactions on Power Delivery*, vol. 6, no. 4, pp. 1629–1640, 1991.

[11] V. Salehi, B. Mirafzal, and O. Mohammed, "Pulse-load effects on ship power system stability," in *IECON 2010 - 36th Annual Conference on IEEE Industrial Electronics Society*, pp. 3353–3358, 2010.

[12] R. Bartelt, M. Oettmeier, C. Heising, V. Staudt, and A. Steimel, "Scenario-based stability-assessment of converter-fed dc-ship grids loaded with pulsed power," in *2011 IEEE Electric Ship Technologies Symposium*, pp. 468–471, 2011.

[13] J. T. Lukowski, W. W. Weaver, and R. D. Robinett, "Time-optimal input-shaping control of a saturating inductor dc-dc converter," in *2018 IEEE 19th Workshop on Control and Modeling for Power Electronics (COMPEL)*, pp. 1–5, 2018.

[14] J. Kaiser and T. Dürbaum, "An overview of saturable inductors: Applications to power supplies," *IEEE Transactions on Power Electronics*, vol. 36, no. 9, pp. 10766–10775, 2021.

[15] V. C. Valchev and A. Van den Bossche, *Inductors and transformers for power electronics*. CRC press, 2018.

[16] R. Bellman, I. Glicksberg, and O. Gross, "On the "bang-bang" control problem," *Quart. Appl. Math.*, vol. 14, pp. 11–18, 1956.

[17] S. V. Dhople, K. A. Kim, and A. D. Domínguez-García, "Time-optimal control in dc-dc converters: A maximum principle perspective," in *2014 IEEE Applied Power Electronics Conference and Exposition - APEC 2014*, pp. 2804–2808, 2014.

[18] J. A. Dillon, W. W. Weaver, R. D. Robinett, and D. G. Wilson, "Electro-mechanical-thermal performance and stability of aircraft energy networks with pulse power loads," *IEEE Transactions on Aerospace and Electronic Systems*, vol. 56, no. 4, pp. 2537–2547, 2020.

[19] R. D. Robinett and D. G. Wilson, "What is a limit cycle?," *International Journal of Control*, vol. 81, no. 12, pp. 1886–1900, 2008.

[20] C. A. Klausmeier, "Floquet theory: a useful tool for understanding nonequilibrium dynamics," *Theoretical Ecology*, vol. 1, pp. 153–161, Sept. 2008.

[21] C. Gökçek, "Stability analysis of periodically switched linear systems using floquet theory," *Mathematical Problems in Engineering*, 2004.

[22] J. A. Álvarez Martín, J. R. Melgoza, and J. J. R. Pasaye, "Exact steady state analysis in power converters using floquet decomposition," in *2011 North American Power Symposium*, pp. 1–7, 2011.

[23] R. Kelly and D. Diaz, "On linearization of a class of nonlinear vector implicit differential equation with application to robotics," in *2016 IEEE International Conference on Automatica (ICA-ACCA)*, pp. 1–6, 2016.

[24] W. W. Weaver and P. T. Krein, "Analysis and applications of a current-sourced buck converter," in *APEC 07 - Twenty-Second Annual IEEE Applied Power Electronics Conference and Exposition*, pp. 1664–1670, 2007.

[25] G. Zhu, B. A. McDonald, and K. Wang, "Modeling and analysis of coupled inductors in power converters," *IEEE Transactions on Power Electronics*, vol. 26, no. 5, pp. 1355–1363, 2011.

[26] H.-J. Byun, J.-M. Park, B.-J. Kim, S.-H. Kim, C.-Y. Won, and J.-S. Yi, "Small signal modeling of interleaved voltage balancer with coupled-inductor," in *2020 IEEE Electric Power and Energy Conference (EPEC)*, pp. 1–6, 2020.

[27] A. Witulski, "Modeling and design of transformers and coupled inductors," in *Proceedings Eighth Annual Applied Power Electronics Conference and Exposition,*, pp. 589–595, 1993.

[28] S. Ćuk and Z. Zhang, "Coupled-inductor analysis and design," in *1986 17th Annual IEEE Power Electronics Specialists Conference*, pp. 655–665, 1986.

[29] A. Witulski, "Introduction to modeling of transformers and coupled inductors," *IEEE Transactions on Power Electronics*, vol. 10, no. 3, pp. 349–357, 1995.

[30] M. Takach and P. Lauritzen, "Survey of magnetic core models," in *Proceedings of 1995 IEEE Applied Power Electronics Conference and Exposition - APEC'95*, vol. 2, pp. 560–566 vol.2, 1995.

[31] Y. Liu and D. Zhang, "Effect of nonlinear inductor behavior on the performance of interleaved power factor correction," *IEEE Transactions on Magnetics*, vol. 48, no. 11, pp. 4143–4147, 2012.

[32] "Wolfram research: Mathematica." https://www.wolfram.com/mathematica/.

[33] P. Krein, *Elements of power electronics*. United Kingdom: Oxford University Press, 1998.

[34] K. Cheng and Y. Lu, "Energy storage for switched mode power converters," in *Proceedings. 2004 First International Conference on Power Electronics Systems and Applications, 2004.*, pp. 38–41, 2004.

[35] B. Lunk and R. Beichner, "Exploring magnetic fields with a compass," *The Physics Teacher*, vol. 49, 2011.

[36] A. Hindmarsh and A. Taylor, "User documentation for ida, a differential-algebraic equation solver for sequential and parallel computers," 01 2000.

[37] A. C. Hindmarsh, P. N. Brown, K. E. Grant, S. L. Lee, R. Serban, D. E. Shumaker, and C. S. Woodward, "SUNDIALS: Suite of nonlinear and differential/algebraic equation solvers," *ACM Transactions on Mathematical Software (TOMS)*, vol. 31, no. 3, pp. 363–396, 2005.

[38] A. C. Hindmarsh, "The pvode and ida algorithms," 12 2000.

[39] M. M. Garg and M. Kumar Pathak, "Performance comparison of non-ideal and ideal models of dc-dc buck converter," in *2018 8th IEEE India International Conference on Power Electronics (IICPE)*, pp. 1–6, 2018.

[40] R. Reddivari and D. Jena, "A detailed model of z-source converter considering parasitic parameters," in *2018 International Conference on Power, Instrumentation, Control and Computing (PICC)*, pp. 1–6, 2018.

[41] B. Yildiz, M. O. Gülbahçe, and D. A. Kocabaş, "Nonideal analysis and voltage mode control of a synchronous buck converter," in *2016 National Conference on Electrical, Electronics and Biomedical Engineering (ELECO)*, pp. 392–396, 2016.

[42] "Curve fit formulas and values - design tools - micrometals." `https://www.micrometals.com/design-and-applications/design-tools/`. Accessed: 2020-06-14.

[43] J. E. Slotine and W. Li, *Applied Nonlinear Control*. Englewood Cliffs, NJ: Prentice-Hall, 1991.

[44] A. Gelb and W. E. V. Velde, "Multiple-input describing functions and nonlinear system design," 1968.